# Atmospheric processing and aerosol aging responsible for observed increase in absorptivity of long-range transported smoke over the southeast Atlantic

5   Abdulamid A. Fakoya[1], Jens Redemann[1], Pablo E. Saide[2,3], Lan Gao[1], Logan T. Mitchell[1], Calvin Howes[3], Amie Dobracki[4], Ian Chang[5], Gonzalo A. Ferrada[6,7], Kristina Pistone[8,9], Sam E. Leblanc[8,9], Michal Segal-Rozenhaimer[13], Arthur J. Sedlacek III[4], Thomas Eck[10,11], Brent Holben[11], Pawan Gupta[11], Elena Lind[11], Paquita Zuidema[12], Gregory Carmichael[14,15] and Connor J. Flynn[1]

10  [1]School of Meteorology, University of Oklahoma, Norman, Oklahoma, USA

[2]Institute of the Environment and Sustainability, University of California, Los Angeles, Los Angeles, California, USA

[3]Department of Atmospheric and Oceanic Sciences, University of California, Los Angeles, Los Angeles, California, USA

15  [4]Environmental and Climate Sciences Department, Brookhaven National Laboratory, Upton, New York, USA

[5]Department of Earth, Environmental, and Geographical Sciences, The University of North Carolina at Charlotte, Charlotte, North Carolina, USA

[6]Cooperative Institute for Research in Environmental Sciences, University of Colorado, Boulder, Colorado, USA

[7]Global Systems Laboratory, National Oceanic and Atmospheric Administration, Boulder, Colorado, USA

20  [8]Bay Area Environmental Research Institute, Moffett Field, California, USA

[9]NASA Ames Research Center, Moffett Field, California, USA

[10]University of Maryland Baltimore County, Baltimore, Maryland, USA

[11]NASA Goddard Space Flight Center, Greenbelt, Maryland, USA

[12]Department of Atmospheric Sciences, Rosenstiel School, University of Miami, Miami, Florida, USA

25  [13]Department of Geophysics, Porter School of the Environment and Earth Sciences, Tel-Aviv University, Tel-Aviv, Israel

[14]Center for Global and Regional Environmental Research (CGRER), University of Iowa, Iowa City, Iowa, USA

[15]Department of Chemical and Biochemical Engineering, University of Iowa, Iowa City, Iowa, USA

*Correspondence to*: Abdulamid A. Fakoya (abdulamid.fakoya@ou.edu) and Jens Redemann (jredemann@ou.edu)

**Abstract.**

35   Biomass burning aerosols (BBA) from agricultural fires in southern Africa contribute about one-third of global carbonaceous aerosol load. These particles have strong radiative effects in the southeast Atlantic (SEA), which depend in part on the radiative contrast between the aerosol layer in the free troposphere (FT) and the underlying cloud layer. However, there is large disagreement in model estimates of aerosol-driven climate forcing due to uncertainties in the vertical distribution, optical properties, and lifecycle of these particles. This study applies a novel method

40   combining remote sensing observations with regional model outputs to investigate the aging of the BBA and its impact on the optical properties during transatlantic transport from emission sources in Africa to the SEA. Results show distinct variations in extinction Ångstrom exponent (EAE) and single scattering albedo (SSA) as aerosol age. Near the source, fresh aerosols are characterized by low mean SSA (0.84) and high EAE (1.85), indicating smaller, highly absorbing particles. By isolating marine contributions from the total column during BBA transport across the SEA,

45   our analysis reveals an initial decrease in BBA absorptivity, with mean FT SSA of 0.87 after 6–7 days, followed by increased absorptivity with mean FT SSA of 0.84 after 10 days, suggesting enhanced absorption due to chemical aging. These findings indicate that BBA becomes more absorbing during extended transport across the SEA, with implications for reducing model uncertainties. Our remote sensing-based results agree well with previous in-situ studies and offer new insights into aerosol-radiation interactions and the energy balance over the SEA.

50

## 1 Introduction

Atmospheric aerosols play a crucial role in Earth's energy balance and climate system. Aerosols perturb the vertical temperature structure, altering the atmospheric stability and overall radiation balance through interactions with sunlight via scattering and absorption, known as aerosol-radiation interactions (ARI) (Ackerman et al., 2000; Boucher, 2015; Santer et al., 1996; Hansen et al., 1997; Koch and Del Genio, 2010; Samset et al., 2018). Aerosols also serve as cloud condensation nuclei (CCN) or ice-nucleating particles (INPs) that influence cloud microphysics and modify cloud reflectivity (Twomey, 1974, 1977) and lifespan (Albrecht, 1989) through aerosol-cloud interactions (ACI) (Ackerman et al., 2000; Boucher, 2015). The resulting impacts of ARI and ACI on climate are cumulatively quantified as climate forcing, and its magnitude and sign depend on several factors, including particle size, composition, concentration, mixing state, optical properties, and vertical distribution at a given location.

Single-scattering albedo (SSA), the ratio of aerosol scattering to aerosol extinction, and an indicator of aerosol absorptivity, is an important parameter in deriving the radiative effects of aerosols (Chylek and Wong, 1995; Takemura et al., 2002; Bergstrom et al., 2007; Satheesh et al., 2010). Non-absorbing aerosols have SSA of 1, whereas absorbing aerosols have lower values (Moosmüller et al., 2012). The magnitude of the direct aerosol radiative effect depends on the interplay between the radiative properties of aerosols and the underlying scene (Keil and Haywood, 2003; Chand et al., 2009). Non-absorbing aerosols more effectively elevate the scene albedo in regions with inherently darker scenes, whereas absorbing aerosols decrease the albedo most strongly over brighter surfaces, with a comparatively lesser impact over darker surfaces (Mishra et al., 2015; Bellouin et al., 2020). On the global average for radiative forcing, absorbing aerosols exert a cooling effect at the top of the atmosphere. In clear-sky maritime scenarios, this radiative forcing is negative. However, when clouds are present in certain regions such as the southeast Atlantic (SEA), the interaction between aerosol and cloud layers can lead to positive radiative forcing, contingent upon the vertical distribution of the aerosols relative to the clouds (Haywood and Shine, 1997; Keil and Haywood, 2003; Chand et al., 2009).

Biomass burning (BB) is the largest source of carbonaceous aerosols globally (Bowman et al., 2009; Vermote et al., 2009; Bond et al., 2013), emitting significant amounts of brown carbon (BrC), light absorbing organic aerosols, and up to 40% black carbon (BC), the strongest light-absorbing aerosol component, into the atmosphere (Bond et al., 2004; Andreae and Gelencsér, 2006; Hopkins et al., 2007; Boucher et al., 2013). The composition of BB aerosols (BBA) is highly variable and often depends on the fuel type and burning conditions, with the less efficient smoldering phase of fires having more organic aerosols (OA) and less BC than the flaming phase (Levin et al., 2010; Liu et al., 2014; Laskin et al., 2015; Jen et al., 2019; Zhou et al., 2017; Collier et al., 2016). BrC exhibits lower mass absorption efficiency compared to BC (Alexander et al., 2008; Jimenez et al., 2009). However, in fires where BrC and BC are co-emitted, the absorption properties of BBA can be influenced by the complex composition which consists of diverse organic compounds capable of oxidation and photochemistry. These reactions, along with particle morphology and the mixing state of the carbonaceous constituents as well as the condensation of gases and other coating materials upon the BC cores can modify the absorptive characteristics and atmospheric residence time of the aerosols (Feng et al., 2013; Saleh et al., 2015; Feng et al., 2021; Dobracki et al., 2023; Lack and Cappa, 2010). Given the projected

global increase in BB events (Keywood et al., 2013; Jones et al., 2022; Tatro and Zuidema, 2025), an understanding of BBA and their spatial and temporal evolution becomes essential to improve the estimate of their climate forcing.

Southern Africa contributes approximately 35% of the global biomass burning emissions (Van Der Werf et al., 2010; Granier et al., 2011; Redemann et al., 2021). Annually, between June and October, these emissions are transported westward over the SEA (Holanda et al., 2020) where they overlie a semi-permanent deck of stratocumulus (Sc) cloud (Figure 1) and occasionally mix into the marine boundary layer (MBL) (Zhang and Zuidema, 2021). Consequently, the region is characterized by heavy periodic loadings of BBA, which represent the global maximum of aerosol optical depth (AOD) above clouds (Waquet et al., 2013; Adebiyi et al., 2015).

BBA in this region typically have SSA values ranging between 0.7 and 0.9 from observations (Dubovik et al., 2002; Haywood et al., 2003; Eck et al., 2013). These values generally increase from July to November (Eck et al., 2013), with an average value of 0.85 during the burning season (Leahy et al., 2007; Eck et al., 2013; Pistone et al., 2019; Dobracki et al., 2023), indicating their significant ability to absorb sunlight. BBA also serve as CCN and account for approximately 65% of the total CCN in the Sc cloud deck of the SEA (Andreae and Rosenfeld, 2008; Dedrick et al., 2024; Che et al., 2021; Lenhardt et al., 2023). The warming effect and the ACI by BBA are not well represented in Earth System Models (ESMs), and the SEA region exhibits a large model-to-model divergence of climate forcing due to aerosols (Sakaeda et al., 2011; Stier et al., 2013; Mallet et al., 2020; Che et al., 2021; Haywood et al., 2021). Reliable quantification of the climatic effects of BBA requires an accurate representation of aerosol properties and their vertical and horizontal distributions in models.

Despite recent studies that have documented the transport and characterized the chemical, optical and microphysical properties of the southern African BBA transport (Denjean et al., 2020a; Pistone et al., 2019; Wu et al., 2020; Baars et al., 2021; Holanda et al., 2020; Denjean et al., 2020b; Vakkari et al., 2018; Dobracki et al., 2023), it is still not well understood how the properties of these aerosols evolve during long-range transport. The southern African BBA have been associated with the BC-rich pollution layer above the Amazonian basin following extended transport over the SEA (Holanda et al., 2020). Variations in the chemical composition of BBA at different altitude above the Atlantic have been shown to influence the optical properties of aged BBA (Wu et al., 2020), with low SSA values attributed to the presence of strongly absorbing refractory black carbon (rBC), and minimal contribution from BrC (Denjean et al., 2020b). The mixing state of rBC particles (Denjean et al., 2020b; Sedlacek et al., 2022) as well as the accumulation of a non-absorbing shell by rBC (Redemann et al., 2001) strongly affect the SSA of BBA. Knowledge of the spatial and temporal evolution of BBA, especially during long-range transport is key to understanding the atmospheric processes affecting their lifecycle and their contribution to climate forcing.

While the aging of BBA has recently been parameterized in global climate models (GCMs) (Konovalov et al., 2021; Nascimento et al., 2021), accurately representing the optical and microphysical characteristics of these particles in models remains a challenge due to the intricate chemical and physical processes involved (Brown et al., 2021) and because there have been limited studies on aged BBA. Most research on the evolution and aging of BBA has focused on BBA that has been sampled near the source or in short-term laboratory experiments (Reid et al., 1998; Bond et al., 2006; Kleinman et al., 2020; Liu et al., 2021; Feng et al., 2021; Sedlacek et al., 2022). Due to the lack of observations on longer time scales, there exists a gap in our understanding of how the optical properties of BBA

change during extended transport, such as that over the SEA. Investigating the evolution of aged BBA is, therefore, crucial for improving model capabilities for representing their optical and radiative properties.

130    The overarching goal of this study is to examine the evolution of BBA emitted during the annual burning season in southern Africa using remote-sensing observations during their transport across the SEA. Studies on BBA in the region have focused primarily on either continental southern Africa (Abel et al., 2003; Eck et al., 2003; Queface et al., 2011; Eck et al., 2013) or over the ocean (Meyer et al., 2013; De Graaf et al., 2014; Zuidema et al., 2018; Pistone et al., 2019; Redemann et al., 2021). Measurements over the ocean from the ORACLES (ObseRvations of Aerosols

135    above CLouds and their intEractionS) campaign dataset highlighted the connection between BBA composition and absorption, showing a decrease in SSA concurrent with the loss of OA coating on rBC particles, as shown by Sedlacek et al. (2022) and Dobracki et al. (2023). However, our study seeks to expand upon these findings by analyzing aerosol absorption along the entire transport pathway of BBA from the emission source to SEA region (Figure 1). Here, we develop a new methodology that integrates remotely sensed observations from AERONET (AErosol RObotic

140    NETwork) in the BB emission region and 4STAR (Spectrometers for Sky-Scanning, Sun-Tracking Atmospheric Research) over the ocean, collected during the ORACLES campaign. These observations are combined with aerosol age estimates outputs from the WRF-AAM (Weather Research and Forecasting coupled with Aerosol Aware Microphysics module) regional model (Saide et al., 2016) and aerosol properties derived from the WRF-CAM5 (Weather Research and Forecasting coupled with the Community Atmosphere Model version 5). WRF-CAM5 has

145    previously been used to document the chemical composition, hygroscopicity and aerosol-cloud interactions of BBA in the ORACLES campaign region (Howes et al., 2023). This approach enables a comprehensive assessment of the aging of the smoke plume and its impact on optical properties. Particularly, we use the observation of BBA from ORACLES campaign during the burning season of September 2016, August 2017 and October 2018, to investigate the changes in SSA of BBA during their transatlantic transport, spanning the phases of transport over land and,

150    subsequently, over the SEA. Furthermore, using remote sensing to retrieve SSA offers the advantage of sampling aerosols in their ambient state and can be replicated to other domains where AERONET observations are available.
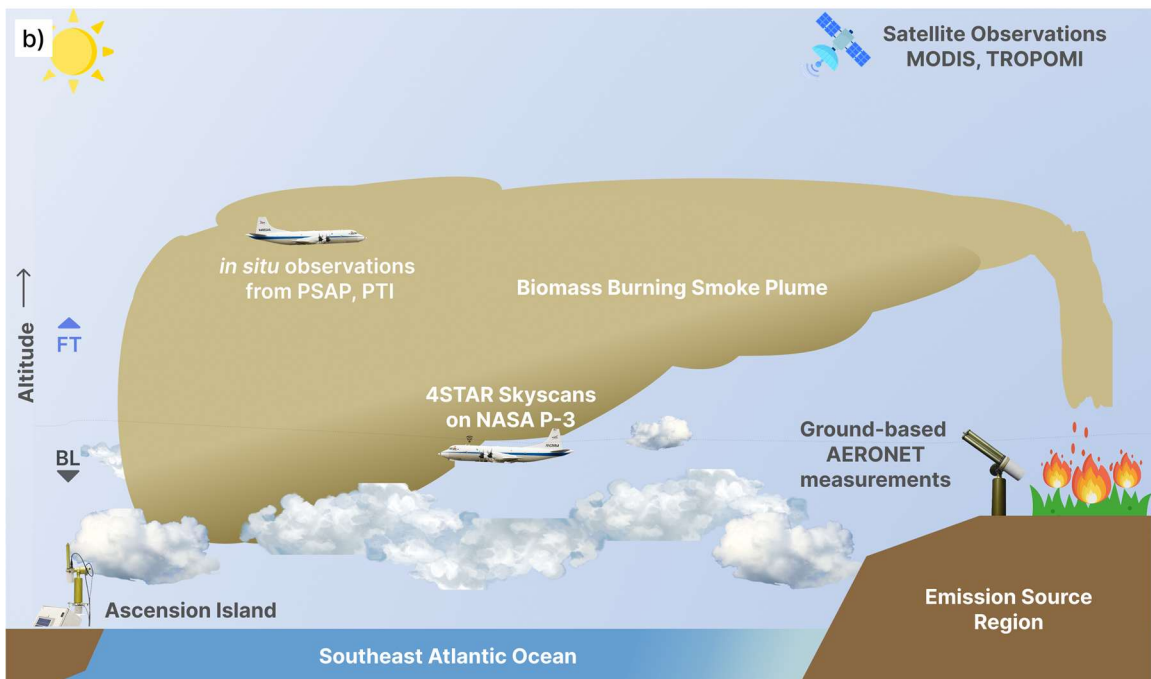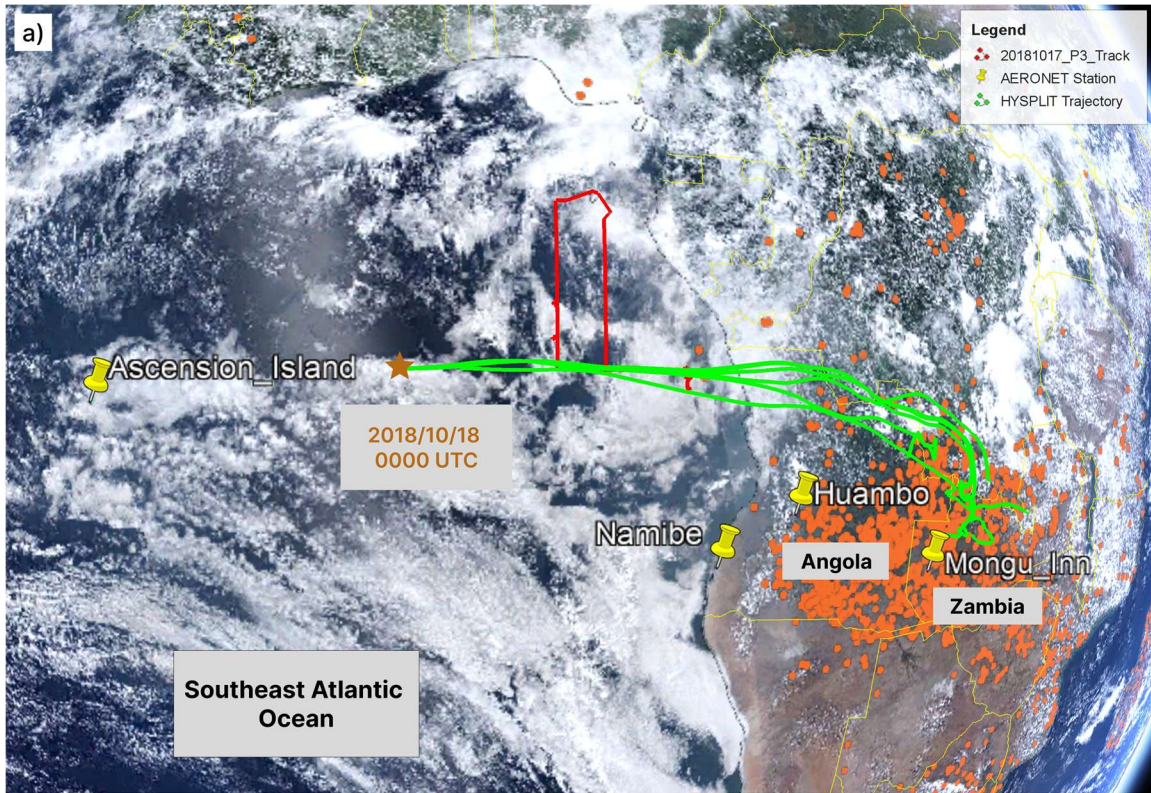
**Figure 1:**

**(a): Satellite image showing the southeast Atlantic Ocean covered by the stratocumulus cloud deck with smoke being advected over it. The smoke from continental fires (orange dots) is being transported, evident by the 7-day backward HYSPLIT trajectory (green) ending between 4000m – 5000m on October 18, 2018, to intersect the P-3 flight (red) on October 17, 2018. Yellow icons represent AERONET stations selected for this study.**

(https://worldview.earthdata.nasa.gov/, https://www.ready.noaa.gov/HYSPLIT_traj.php, https://earth.google.com, https://aeronet.gsfc.nasa.gov/).

**(b): Schematic of the collocation of observations in the southeast Atlantic region during the ORACLES mission. Satellite observation from Moderate Resolution Imaging Spectroradiometer (MODIS) and TROPOspheric Monitoring Instrument (TROPOMI). Airborne observations from 4STAR, ground-based observations from AERONET, in-situ measurement from Particle Soot Absorption Photometer (PSAP) and Photo-Thermal Interferometric (PTI) Particle Absorption Monitor. Measurements from 4STAR and AERONET are presented in this study.**

## 2 Data and methods

### 2.1 NASA ORACLES campaign

A comprehensive overview of the ORACLES campaign is presented by Redemann et al. (2021); Here, we summarize the methods and data analysis techniques that are relevant to this study. The campaign provided process-level understanding of aerosol effects in the SEA that can be applied in the parameterization of ACI and ARI in ESMs (Redemann et al., 2021). The campaign overlapped with other field experiments (Zuidema et al., 2016) – CLARIFY-2017: Cloud-Aerosol-Radiation Interactions and Forcing for Year 2017 (Haywood et al., 2021), LASIC: Layered Atlantic Smoke Interactions with Clouds (Zuidema et al., 2018), AEROCLO-sA: AErosols, RadiatiOn and CLOuds in southern Africa (Formenti et al., 2019) – in a synergistic effort to determine the influence of southern African BBA on cloud properties and the energy balance in the SEA region. The ORACLES campaign occurred between 2016 and 2018 with field deployments in Walvis Bay, Namibia (September 2016), and in São Tomé and Principe (August 2017, and October 2018). The NASA P3-B aircraft was home to a suite of in-situ and remote-sensing instruments including the 4STAR (Dunagan et al., 2013) and the ER-2 (a high-altitude aircraft) was home to a suite of additional remote sensing instruments. A total of 56 research flights:12 from the ER-2, only in 2016, and 44 from the P-3B across the three deployments, shown in Figure 2, with over 450 science flight hours, collected data on aerosol optical properties (Pistone et al., 2019; Redemann et al., 2021). This study uses 4STAR retrievals of BBA properties (Table 1) from all three campaign deployments made on the P-3B aircraft, to study the evolution of light absorption properties of BBA.
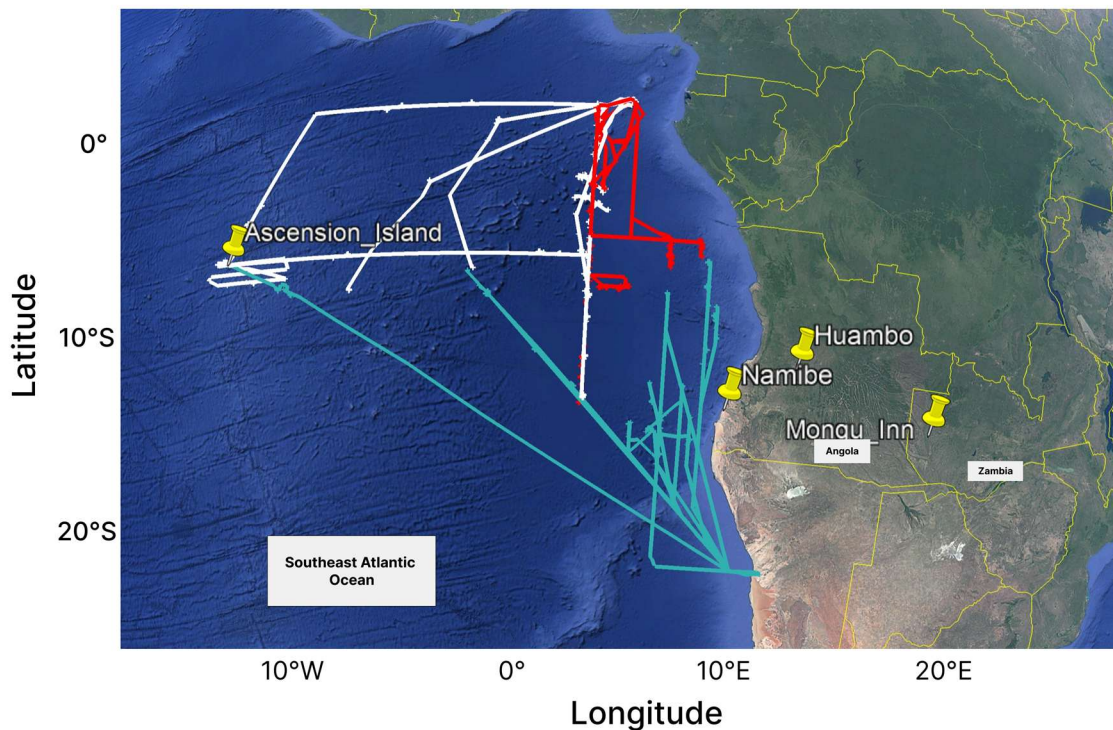
**Figure 2: Map of the SEA showing the NASA P-3B flight tracks during ORACLES 2016 (cyan), 2017 (white) and 2018 (red) for observation days analyzed in this study. The ORACLES aircraft deployed out of Walvis Bay, Namibia in 2016 and São Tomé and Príncipe in 2017 and 2018. Regional AERONET stations are identified using yellow icons. Background imagery from Google Earth (https://earth.google.com) - Data SIO, NOAA, U.S. Navy, NGA, GEBCO, Image Landsat / Copernicus.**

## 2.2 Ground-based measurements

AERONET, a global sun photometer network, provides long-term, continuous measurement of AOD and retrievals of aerosol microphysical, optical, and radiative properties for aerosol characterization and validation of satellite retrievals (Holben et al., 1998). In this study, we used AERONET Version 3 inversion products (Table 1) from both almucantar (ALM) and hybrid scans including cloud-screened (level 1.5) and quality assured (level 2.0) data (Giles et al., 2019; Sinyuk et al., 2020) from four AERONET stations: three situated in continental southern Africa, **Mongu Inn (Zambia), Huambo (Angola), Namibe (Angola)**; and one in the maritime SEA - **Ascension Island (United Kingdom Territory)** (Table 2). These stations were carefully selected based on their geographic locations aligning with the trajectory of BBA from continental Africa and over the ocean, as shown in Figure 1. Specifically, column-integrated measurements of AOD, SSA, and extinction Ångstrom exponent (EAE) for September 2016, August 2017, and October 2018 were used, coinciding with the observation periods of ORACLES 2016, 2017, and 2018. The Namibe site was inactive during the ORACLES 2018 campaign, providing data only for 2016 and 2017, while the Huambo site, established in 2017, contributed observations for both 2017 and 2018. At Ascension Island and Namibe, fewer observations were available due to the increased cloud cover along the coast and

over the SEA. Therefore, to ensure an adequate sample size at Ascension Island and Namibe, we included level 1.5 data in our analysis when level 2.0 data was unavailable. More information about the AERONET stations utilized in this study is provided in Table 2.

**Table 1: Summary of observation data products and aerosol properties used in this study.**

| Data | Product | Properties | Data Access |
|---|---|---|---|
| **AERONET** | Inversion (level 1.5, 2.0) product version 3: All Observation | Aerosol Optical Depth (AOD) & Single Scattering Albedo (SSA) *440, 675, 870 nm* Extinction Ångstrom Exponent (EAE) *440-870 nm* | https://aeronet.gsfc.nasa.gov/ |
| **4STAR** | 4STAR-aeroinv_P3 | Aerosol Optical Depth (AOD) & Single Scattering Albedo (SSA) *500, 675, 870, 975 nm* Extinction Ångstrom Exponent (EAE) *500-975 nm* | https://espoarchive.nasa.gov/ archive/browse/oracles/P3/4S TAR-aeroinv |

210

### 2.3 Airborne measurements

This study uses sky radiance measurements from the airborne 4STAR instrument (Dunagan et al., 2013) aboard NASA P-3B aircraft, enabling AERONET-like observations in remote regions beyond ground-based network coverage. Its frequent co-deployment with in-situ instrumentation offers a more comprehensive characterization of aerosol properties. This analysis focuses on observations made in the sky-scanning mode (Pistone et al., 2019), using both ALM and principal plane (PPL) scans. Given that most ORACLES flights occurred near solar noon, limiting the angular range of ALM scans, PPL scans were selectively included if they met specific quality control (QC) criteria. Here, we processed 4STAR sky scans using the QC criteria from Mitchell et al. (2023). These criteria were adapted from Pistone et al. (2019) for four-wavelength 4STAR retrieval of ORACLES 2016-2018 and serve as a proxy for AERONET level 1.5 aerosol inversion standards. The criteria are: (1) AOD (400 nm) > 0.2, (2) altitude difference < 50 m, (3) sky error < 10%, (4) minimum scattering angle < 6°, (5) maximum scattering angle > 50°, (6) mean scattering angle difference < 3° (between 3.5 and 30°), (7) maximum scattering angle difference < 10° (between 3.5 and 30°), (8) roll standard deviation < 3°, (9) passes retrieval boundary test - ensuring that the retrieval is within limits of parameter space, and (10) maximum altitude < 3000 m. A summary of the valid QC'd 4STAR retrievals of SSA, AOD, EAE (Mitchell et al., 2023) in the ORACLES dataset (Oracles, 2020) for all three deployments is given in Table 1.

**Table 2: Site information and total observation count for AERONET and 4STAR.**

| Site Name | Latitude | Longitude | Elevation (m) | Number of Observations *(2016, 2017, 2018)* |
|---|---|---|---|---|
| Ascension Island | -7.97 | -14.41 | 30 | 77 *(17, 53, 7)* |
| Namibe | -15.15 | 12.17 | 11 | 135 *(71, 64, -)* |
| Huambo | -12.86 | 15.7 | 1670 | 342 *(-, 250, 92)* |
| Mongu Inn | -15.26 | 23.13 | 1040 | 444 *(126, 167, 151)* |
| 4STAR | - | - | - | 308 *(77, 139, 92)* |

230

### 2.4 WRF-CAM5: Concept and Configuration

WRF-CAM5 is an adaptation of the WRF-Chemistry (WRF-Chem) model (Grell et al., 2005), which integrates the physics and aerosol packages of the global CAM5 (Ma et al., 2014; Zhang et al., 2015a), making it suitable for studying multi-scale atmospheric processes and evaluating aerosol and physics parameterizations in global climate models (Wang et al., 2018). WRF-CAM5 has been widely applied to investigate air quality and climate interactions in Asia and the United States (Campbell et al., 2017; Wang et al., 2018; Zhang et al., 2015b) and has shown good skill in capturing smoke concentration, aerosol properties, and the vertical distribution of BBA in the SEA region (Doherty et al., 2022; Chang et al., 2023). In this study, the model is configured at 36km horizontal resolution with 74 vertical layers over the spatial domain 41°S-14°N, 34°W-51°E, initialized every five days using the National Centers for Environmental Prediction (NCEP) Final Operational Global Analysis (NCEP FNL) and Copernicus Atmosphere Monitoring Service (CAMS) reanalysis datasets as detailed in Shinozuka et al. (2020a) and Doherty et al. (2022), with daily smoke emissions from the Quick-Fire Emissions Dataset version 2 (QFED2) (Darmenov and Da Silva, 2015).

### 2.5 Plume Age Derivation

To estimate the age of the aerosols, defined as the time since emission, we utilized carbon monoxide (CO) tracer coupled with smoke emissions within the WRF-AAM model. The WRF-AAM model, which share similar configurations with WRF-CAM5, allows for region- and case-specific microphysical parameterization of aerosol-cloud interactions (Thompson and Eidhammer, 2014) and aerosol-radiation interactions (Saide et al., 2016), thus facilitating the characterization of aerosol aging processes.

The regional model was set up with a horizontal resolution of 12 km, encompassing the geographical area (41°S-14°N, 34°W-51°E). This domain size is considered sufficiently extensive to contain nearly all fires across the African continent (Saide et al., 2016; Howes et al., 2023). The fire emission source for the model is based on QFED2 which uses fire radiative power (FRP) as a proxy for estimating fire emissions. QFED2 leverages the cloud correction techniques developed in the Global Fire Assimilation System (GFAS) to refine emission estimates (Darmenov and

Da Silva, 2015). Location and FRP of fires are sourced from MODIS Level 2 fire products (MOD14 and MYD14), coupled with MODIS Geolocation products (MOD03 and MYD03). The NCEP Global Forecasting System (GFS) meteorology serves as the primary driver for the WRF-AAM model which incorporates daily smoke emissions from QFED2, which are subsequently adjusted to correspond with satellite-derived AOD using a near real-time inversion algorithm, as detailed in Saide et al. (2016).

The model was run in a forecast mode to estimate the time since smoke emission, with a maximum aerosol age of 14 days. The model attaches age tracers to the CO released at BB emission sites. These tracers, which are treated as chemically inert gases, are tagged for each day, and tracked for up to two weeks, allowing sufficient time for the smoke to travel across the SEA. This model setup operates in a cycle, where each day, the tracers from the previous day are shifted to the next older tracer bin, continuing until they reach the 14-day mark. At this point, they accumulate in the oldest bin. The age of the smoke plume is determined by averaging the concentration of these tracers at any given location. However, this setup has limited accuracy at the upper end of the age estimate; for instance, smoke older than 14 days is still averaged as 14 days old, even if it contains an equally concentrated mixture of tracers that have been out for different lengths of time beyond the 14-day tracking period. In comparison, the HYSPLIT model (Stein et al., 2015), also driven by the NCEP GFS meteorology, typically yields age estimates that are approximately one day lower than the WRF-AAM. Given that HYSPLIT employs a simpler scheme at coarser resolutions, it is likely that the age estimates from WRF-AAM model are more accurate and reliable. The plume ages assigned within a given column exhibited minimal variability (see supplemental information S6), which gives confidence to the method.

To determine the effective aerosol age for AERONET and 4STAR observations, which are columnar, the WRF-AAM model's assigned plume age in the vertical layers above these instruments is weighted by their respective extinction coefficients ($\beta\_ext$) per equation (1):

$$Aerosol\ age = \frac{\int_{s_{elv}}^{toa} \beta_{ext} * plume\ age\ dz}{\int_{s_{elv}}^{toa} \beta_{ext}\ dz} , \tag{1}$$

Where $s_{elv}$ is the elevation of the AERONET station or the flight altitude of observation for 4STAR and toa is the top of the atmosphere.

**2.6 Spatiotemporal Collocation and Analysis**

The AERONET inversion products provide AOD and SSA at four wavelengths: 440, 675, 870, and 1020 nm. The relationship between AOD and wavelength, defined by the Ångström exponent formula (Eck et al., 1999) is used to compute EAE($\alpha$):

$$EAE(\alpha) = -\frac{\ln(\tau_1) - \ln(\tau_2)}{\ln(\lambda_1) - \ln(\lambda_2)}, \tag{2}$$

Where $\tau_1$ and $\tau_2$ are AOD at wavelengths $\lambda_1$ and $\lambda_2$. In AERONET and 4STAR retrievals, EAE($\alpha$) is calculated from AOD measurements at 440 nm and 870 nm.

Given the differences in the temporal resolution of 4STAR and AERONET observations and the WRF-AAM model outputs, we adapted the model output to match all AERONET and 4STAR observations spatially and temporally, to yield the extinction-weighted aerosol age calculated using extinction at 532 nm as in Equation (1). However, since AERONET does not provide retrievals at 532 nm, we computed the equivalent AOD and SSA at 532 nm to correspond with the model's output using the Ångström formula (equation 2) for AOD, and the linear interpolation equation for SSA.

**2.7 Separating Boundary Layer (BL) contributions from Total Column (TC) observations**

As sea surface temperatures increase, the boundary layer (BL) deepens offshore before transitioning to a cumulus regime (Zhang and Zuidema, 2019, 2021; Ryoo et al., 2021). Continental BBA are lofted above 6 km and advected above the cloud layer by free troposphere (FT) winds (Ryoo et al., 2021), particularly during strong south African Easterly Jet (AEJ-S) episodes (Adebiyi and Zuidema, 2016). Although generally elevated, subsidence (Wilcox, 2010) and low-level easterlies (Diamond et al., 2018) can entrain BBA into the BL between June and August, altering aerosol properties (Dobracki et al., 2025).

Dang et al. (2022) showed that BBA sampled during ORACLES dominate the FT while sea salt aerosols may often dominate the BL over the SEA with a fraction of BBA mixed with sea salt aerosols in the BL. Therefore, our goal of investigating the evolution of BBA from TC observations is complicated by the potential contribution of non-BBA aerosols from the MBL. To address this and given that AERONET and 4STAR provide columnar retrievals above the observation altitude, we employed a two-pronged approach, detailed in Section 2.7.1 and 2.7.2, to isolate the FT aerosol from the columnar observations. First, we applied a model-derived ratio to partition aerosol loading in the FT and BL over the SEA. Subsequently, we implemented a size thresholding technique to exclude contributions from larger particles, ensuring our analysis remains focused on BBA properties.

**2.7.1 Application of model-derived extinction ratio**

To address the potential influence of MBL aerosol properties on the TC observations by AERONET and 4STAR over the SEA, we use a model-derived vertical distribution of extinction to estimate the FT contributions to the TC measurements, while assuming an external mixing state of particles over the ocean. Specifically, we applied model-derived ratios of extinction in the BL relative to the TC ($R_{BL}$), and in the FT relative to the TC ($R_{FT}$) to:

(i) all AERONET observation at Ascension Island and Namibe;
(ii) 4STAR observations when the NASA P-3 aircraft was flying within the BL.

To compute $R_{BL}$ (equation 3) and $R_{FT}$, we applied BLH values from WRF-CAM5 for both sets of observations. The BLH values are estimated according to (Chang et al., 2023) and validated with radiosonde observations at Ascension Island (Zhang and Zuidema, 2019).

$$R_{BL} = \frac{\int_{s_{elv}}^{BLH} \beta_{ext} dz}{\int_{s_{elv}}^{toa} \beta_{ext} dz},$$ (3)

$$R_{FT} = 1 - R_{BL}, \tag{4}$$

320  Using the computed ratios, we partitioned the columnar AOD ($AOD_{TC}$) measurements at locations (i) and (ii)using the following equations:

$$AOD_{BL} = R_{BL} * AOD_{TC}, \tag{5}$$

$$AOD_{FT} = R_{FT} * AOD_{TC}, \tag{6}$$

Here, $AOD_{BL}$ and $AOD_{FT}$ represent the partial AOD at 532 nm within the BL and FT, respectively. For (i), $AOD_{TC}$
325  refers to the columnar AOD above the site's elevation and $AOD_{BL}$ represents the portion of AOD between that elevation and the BLH. For (ii), $AOD_{TC}$ refers to the columnar AOD above the P-3 aircraft altitude, while $AOD_{BL}$ represents the portion of AOD between the P-3 flight altitude and the BLH.

We next calculated the proportion of aerosol age and SSA within the FT using the following:

$$Aerosol_{age_{FT}} = \frac{\int_{BLH}^{toa} \beta_{ext} * \text{plume age dz}}{\int_{BLH}^{toa} \beta_{ext} \, dz}, \tag{7}$$

330  $$SSA_{FT} = \frac{(SSA_{TC} * AOD_{TC}) - (SSA_{BL} * AOD_{BL})}{AOD_{FT}}, \tag{8}$$

While the WRF-CAM5 BLH values generally agree with observational data, our analysis indicates that the model significantly underestimates aerosol loading in the BL, a limitation also highlighted in prior studies (Figure 8-11, Doherty et al. (2022)). Despite having the most accurate model representation of aerosol properties in the SEA region (Doherty et al., 2022), this underestimation in the BL by WRF-CAM5 (see supplemental Figures S7 – S9)
335  affects the representation of BBA properties in the FT at location (i) and (ii) , with physically unrealistic values. To address this, we applied an assumed $SSA_{BL}$ value of 1, recognizing that this introduces a source of uncertainty to the analysis, as it assumes that all aerosols in the BL are purely scattering and does not account for the occasional mixing of BBA with marine sea salt in the BL. To aid the separation of BL and FT BBA, we applied an EAE screening, described below.

340  **2.7.2 Application of Extinction Ångstrom Exponent (EAE) Thresholds**

The extinction Ångstrom Exponent (EAE) is sensitive to the size distribution of aerosol particles (Eck et al., 1999; Schuster et al., 2006; Aladodo et al., 2022). Fine-mode aerosol particles, such as smoke typically have a higher EAE (usually > 1) than coarse-mode aerosols such as marine sea salt, which typically have a lower EAE (< 1). Along with implementing the model-derived extinction ratio outlined in Section 2.7.1, to further discard contributions of
345  other aerosols to the columnar measurements, particularly in atmospheric layers above location (i) and (ii), we applied an EAE filter. We posit that EAE values < 1 would indicate the presence of sea salt aerosol whereas EAE values $\geq$ 1.5 would indicate the dominance of BBA (Eck et al., 1999) while layers with measured EAE values between 1 and 1.5 contain varying degrees of sea salt and BBA following the results of Dang et al. (2022). We tested four EAE threshold values: $\geq 0.75, \geq 1, \geq 1.2,$ and $\geq 1.4,$ to successively exclude such measurements, retaining only fine particles

350 while carefully considering the data processing. Our analysis of the EAE thresholding (see supplemental information S3 for more details) suggests that EAE of 1.5 for BBA might be applicable near emission sources, lower values during transport and aging led us to choose a lower threshold of 1.2 to have more robust statistics over the ocean.

## 3 Results and Discussion

### 3.1 Age distribution of smoke plumes

355 The aerosol age (a) and extinction (b) on October 17, 2018, as derived by the WRF-AAM model is shown in Figure 3, with the altitude track of the P-3 aircraft, which flew over the SEA between 7:00 – 15:00 UTC (see also supplemental Figure S10), overlaid onto the curtain plot. For this case, the model simulates particles at altitudes below 2 km and above 8 km to be substantially older, with plume age ranging from 9 – 12 days, than those in the mid FT (3 – 7 km) with age ranging from 3 – 8 days. The age of the plume sampled between 12:00 – 13:00 UTC at the flight

360 intersection with the HYSPLIT trajectory shown in Fig. 1 ranged from 4 – 8 days, relative to HYSPLIT age range of 4 – 6 days (see supplemental Figure – S1). In Figure 3(b), the vertical distribution of aerosol extinction generally revealed maximum extinction within the lowest 2km. The model demonstrated a consistent inverse relationship between extinction and height, with extinction decreasing as height increased, reaching a minimum above 6 km.

**a. Curtain Plot of Age on 2018-10-17**

**b. Curtain Plot of Extinction at 532 nm on 2018-10-17**
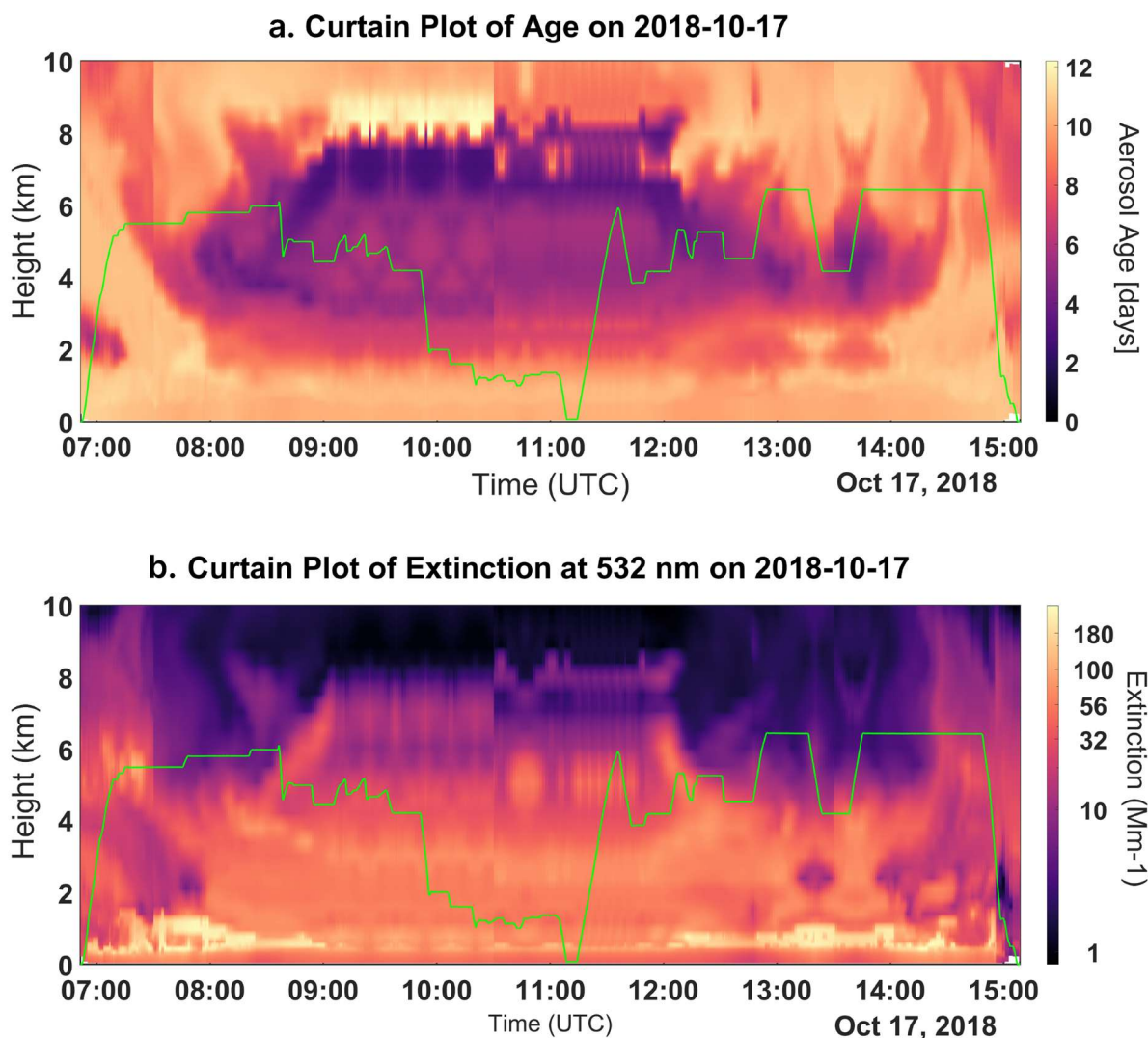
**Figure 3: WRF-AAM curtain plot with altitude on the Y-axis and time in UTC on the X-axis, showing the smoke plume age forecast (a) and aerosol extinction (b) along the P-3 track (solid green line) during research flight 10 of the third ORACLES deployment on October 17, 2018. The smoke plume age is calculated as the average of the tracer concentration in each age bin.**

The modeled vertical distribution of aerosol age and extinction across all ORACLES flight missions and exemplified in Fig. 3 reveals a distinct pattern: aerosols around 7km, within a central altitude band of 3 – 8 km, are younger and likely represent aerosols recently transported by the FT jet. In contrast, aerosols below 1 km and above 8 km over the ocean appear to have an older connection to their source regions, suggesting they either followed a different transport route than the FT aerosols or were recirculated by the AEJ-S, as previously described by Adebiyi and Zuidema (2016).

The distribution of aerosol age from all AERONET and 4STAR observations considered in this study (Fig. 4) show the oldest BBA are observed near Ascension Island (7.9°S, 14.4°W), a remote island about 2000 km away from the African coast. WRF-AAM outputs predict the samples at Ascension Island to be aged between approximately

7 – 12 days, with a mean age of approximately 10 days, while for 4STAR observations, WRF-AAM show that the aerosol age ranged between 3 and 12 days, with a mean age of about 7 days. However, younger BBA were observed over land, closer to the source region of the fires. The plumes sampled at Mongu, Huambo, and Namibe, were aged between 1 – 7 days, 0 – 6 days, and 3 – 9 days, respectively, with mean age of approximately 4, 3.5, and 6 days. The youngest aerosols in the source region were sampled at Huambo (12.8°S, 15.7°E) and Mongu (15.2°S, 23.1°E), with over 75% of all observations at both stations aged less than 4 days. The mean age of aerosols near the African coast was approximately 6 days, suggesting that the smoke measured at Namibe (15.15°S, 12.17°E) has migrated from the primary burning region at Mongu and Huambo. This is further supported by trajectory analysis (see supplemental Figure S1) and by the limited count of active fires recorded in the vicinity of Namibe during the campaign period as shown in Fig. 1. 4STAR observations show a wider age range than those from AERONET sites. This variability is likely attributed to the ORACLES flight strategy, which sometimes targeted freshly emitted smoke from new fires, resulting in the lower age range of 3 to 6 days. The modeled aging pattern suggests the smoke originating from the continent follows a relatively steady trajectory up to Ascension Island. This is supported by HYSPLIT trajectory analysis (see supplementary information – S2), which reveals that the majority of air masses from the burning region follow a similar path westward, typically reaching Ascension Island within 10 to 12 days.
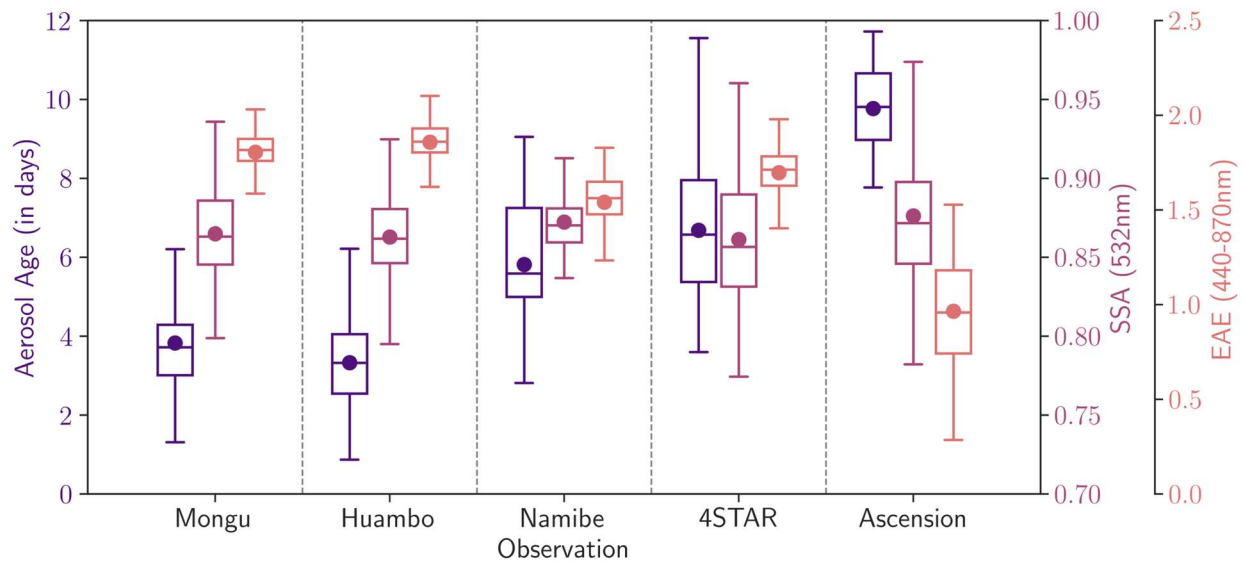
**Figure 4: Box and whisker plots showing the distribution of aerosol age (violet), SSA$_{532nm}$ (magenta) and EAE (peach) in the TC for available observation at each site. The box-whisker plot shows the 10th (lower whisker), 25th (lower box), 50th (median), 75th (upper box), and 90th (upper whisker) percentiles. The mean value for each parameter is marked with the circle.**

**3.2 Changes in total column SSA with age**

Next, we investigate the relationship between SSA and the model-derived age, stratified by the EAE in the TC over the entire study region. We do this by combining the available collocated AERONET, 4STAR and WRF-AAM output datasets from September 2016, August 2017, and October 2018. Combining data from all three months

together provides additional dynamic of change in SSA with time through the burning season months as shown in Eck et al. (2013). The distribution of SSA and EAE by observation site is shown in Fig. 4, while Figure 5 shows SSA at 532 nm and EAE as a function of model-derived aerosol age for all observations in the TC. The cluster of high-EAE data, seen between 0 to 4 days in Fig. 5, is primarily made up of measurements in the burning region from Mongu and Huambo, with average EAE values of 1.81 and 1.86, respectively (Fig. 4), indicating a dominance of BBA in the TC at these locations. Correspondingly, the TC SSA ranges between 0.77 and 0.97, with mean TC SSA of 0.86 at the two locations, with over 75% of the data below 0.90.
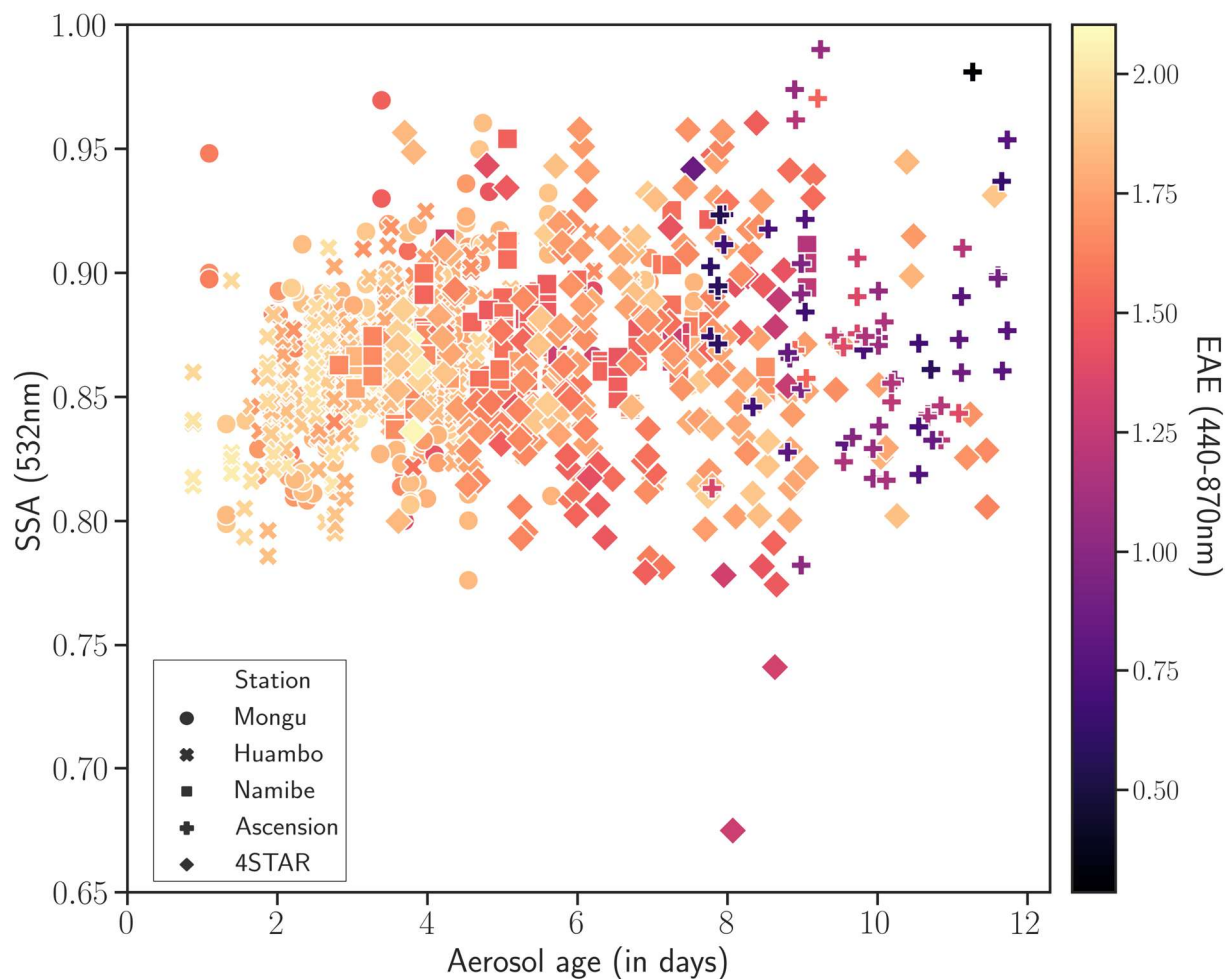
**Figure 5: Relationship between SSA$_{532nm}$ (y-axis), EAE (color bar), and aerosol age (x-axis) in the total atmospheric column (TC). The different markers represent the site of observation while the marker shading represents the EAE.**

The TC SSA result in the source region at Mongu and Huambo implies that fresh BBA (≤ 4 days) is optically dark and highly absorbing of solar radiation as indicated by low SSA values (Table 4), which is consistent with previous findings (Haywood et al., 2003; Abel et al., 2003; Leahy et al., 2007; Eck et al., 2013) in the region. A decrease in TC EAE is observed with increasing distance from the source region (see supplemental Figure S14),

indicating larger particle sizes at more remote locations over the SEA. At Namibe, the mean TC EAE is 1.54, with a mean TC SSA of 0.87, ranging from 0.83 to 0.95. This observed trend of increasing particles size align with in-situ

420    aerosol size measurements (Howes et al., 2023). Aerosols over the SEA exhibit a broad range of TC EAE values, from 0.28 and 2.0, reflecting significant heterogeneity in particle sizes within the TC. These observations have a mean TC SSA of 0.86 for 4STAR, with a range between 0.67 – 0.96, and a mean TC SSA of 0.87 at Ascension Island, ranging from 0.78 to 0.99. Some retrievals over the SEA showed both low SSA values (< 0.8) and low EAE values (≤ 1.0), suggesting the possible presence of other aerosol types at Ascension Island (Howes et al., 2023), or a combination of

425    coarse non-or less-absorbing particles and BBA within the same column.

Upon applying an EAE threshold of 1.2 to the TC, we binned the aerosol age into two-day intervals and estimated the mean TC SSA for each bin (Fig. 6). The result shows that mean TC SSA increases with age, changing from 0.84 within 0 to 2 days of emission over land in the source region up to 0.87 after 6 to 8 days, then decreases over the ocean, reaching approximately 0.86 after 10 to12 days. This result indicates changes in aerosol optical

430    properties during different stages of transport.
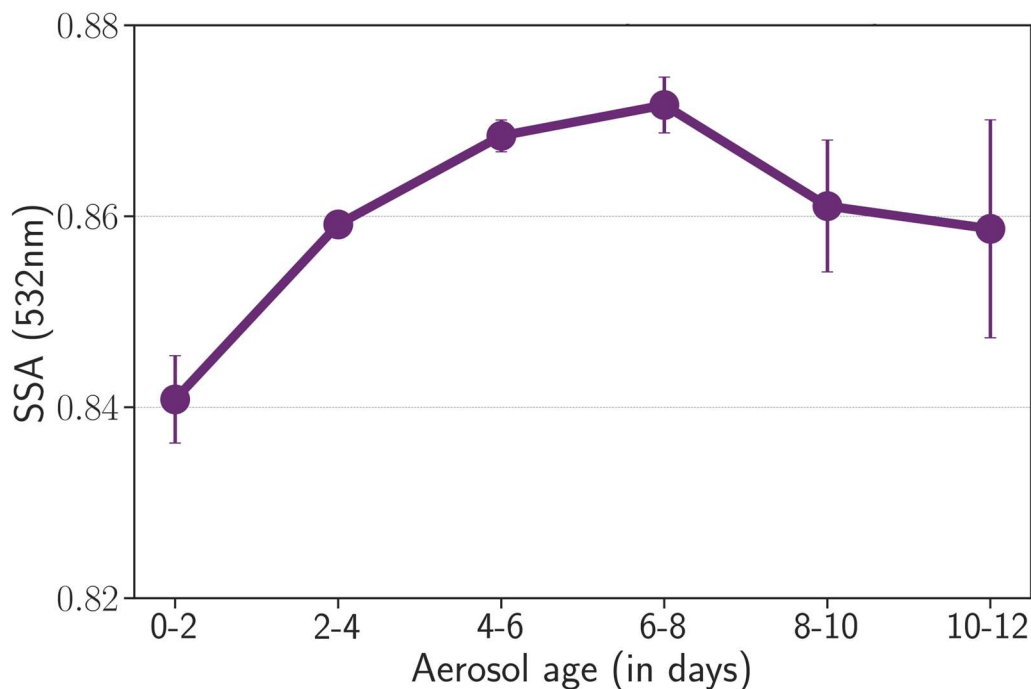
**Figure 6: Mean SSA (at 532 nm) within the vertical column (TC SSA) as a function of aerosol age for the optimal threshold (EAE ≥ 1.2). Error bars represent the standard error of the mean.**

### 3.3 Vertical partitioning of aerosol properties.

435    In this section, we present and analyze the results of the vertical partitioning of aerosol properties, utilizing the model-derived extinction ratio as outlined in Section 2.7.1. Through this method, we made comparisons between the optical properties of aerosols residing in the FT and those in the TC, providing insights into the distribution of aerosols across the two layers.

### 3.3.1 Free Tropospheric Aerosol Loading

440         The fraction of AOD in the free troposphere (FT AOD) relative to the total column AOD (TC AOD) over the SEA, derived from the WRF-CAM5 model, is shown in Figure 7. For AERONET, TC AOD represents the columnar AOD above the site elevation, while for 4STAR, TC AOD refers to the AOD above the aircraft altitude. The modeled FT AOD fraction exhibits considerable spatial variation, with contributions to TC AOD ranging from 0.42 to 0.92 (mean: 0.73) at Ascension Island, 0.68 to 0.99 (mean: 0.95) for 4STAR observations, and 0.70 to 0.95

445 (mean: 0.86) at Namibe. Only 4STAR sky scans conducted at flight altitudes below the BL top were included in the separation, representing approximately 48% of the total 4STAR sky scans. The differences in the fraction of FT AOD between Ascension Island, 4STAR, and Namibe (as shown in Fig. 7) can be attributed primarily to the relative proximity to the source regions. The 4STAR measurements, taken predominantly east of Ascension Island, captured denser smoke plumes before they reached the island. Additionally, the higher FT AOD in 4STAR compared to

450 AERONET is likely due to unaccounted AOD between the aircraft altitude and the surface in the 4STAR dataset. This finding emphasizes that a substantial portion of TC AOD, exceeding 50% on average resides in the FT, indicating a higher aerosol loading in the FT compared to the MBL over the SEA. Subsequently, the model-derived fraction (Equation 4) is applied to estimate FT AOD for Ascension Island, 4STAR and Namibe retrievals using Equation (6). At Ascension Island, the mean FT AOD for the campaign period is approximately 0.23 compared to the mean TC

455 AOD of 0.31, as shown in Figure 8 and summarized in Table 3. However, higher mean FT AOD values of 0.35 and 0.76 are observed from 4STAR and at Namibe, respectively. The FT AOD from 4STAR aligns with findings of Shinozuka et al. (2020b) who reported that daytime AOD above-cloud is similar to that in clear-sky conditions over the SEA. The observed FT aerosol loading from AERONET and 4STAR measurements over the SEA ocean agrees with the modeled FT AOD reported in Chang et al. (2023) for the same region.
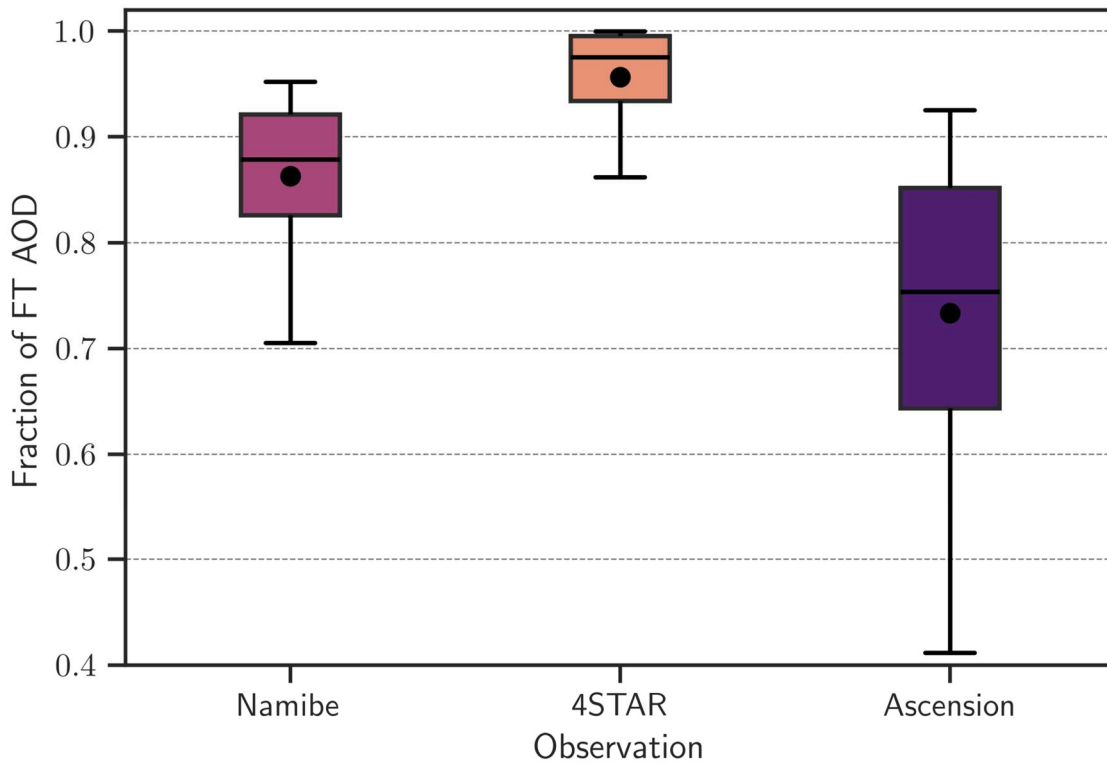
460

**Figure 7: Model-derived fraction of free tropospheric (FT) AOD to total column (TC) AOD. A fraction of 1 means that aerosol loading is completely in the FT. The box-whisker plot shows the 10th (lower whisker), 25th (lower box), 50th (median), 75th (upper box), and 90th (upper whisker) percentiles of fraction of FT AOD. The black circle represents the mean fraction. Note: the outliers have been hidden in the figure. Therefore, on average, more than 50% of the aerosol loading in the ORACLES observation region is in the FT.**

465
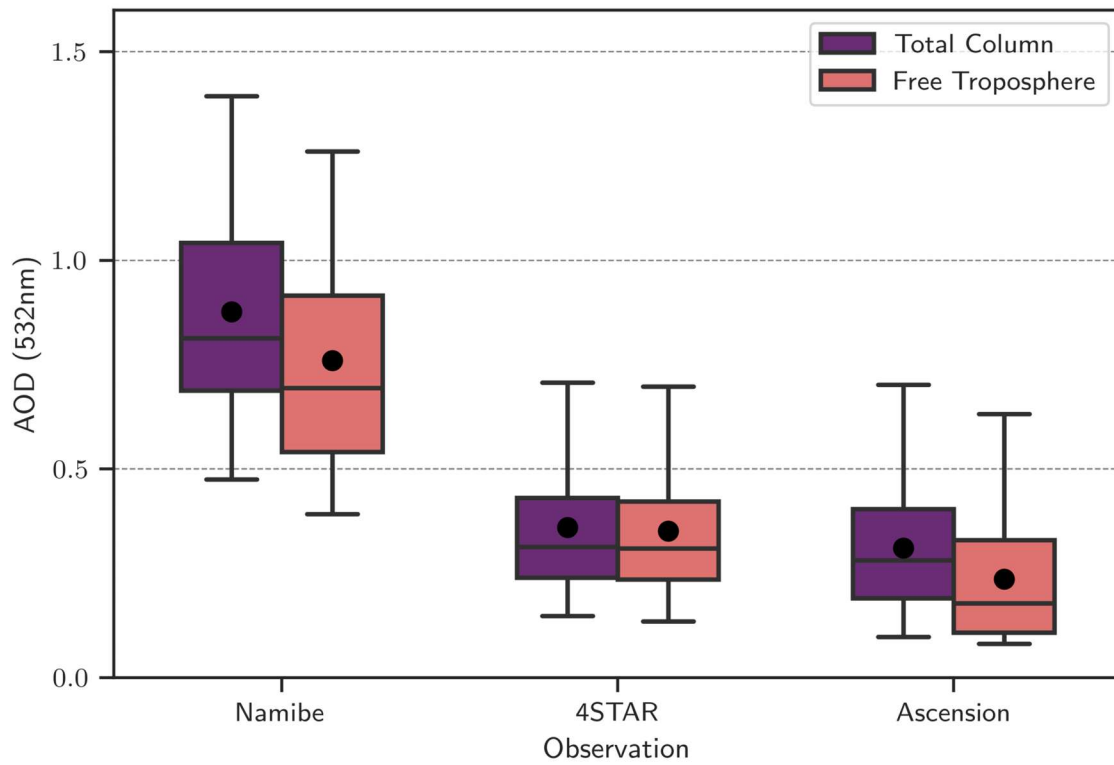
**Figure 8: Comparison of AOD (at 532 nm) in the total column (TC) and free troposphere (FT) over the southeast Atlantic (SEA) ocean. The box-whisker plot shows the 10th (lower whisker), 25th (lower box), 50th (median), 75th (upper box), and 90th (upper whisker) percentiles. Solid black circles represent mean AOD values.**

470

**Table 3: Summary statistics of (a) Fraction of FT AOD (b) TC AOD and FT AOD (c) TC EAE and FT EAE.**

| (a) Fraction of FT AOD | | | | | | | | |
|---|---|---|---|---|---|---|---|---|
| Site Name | Count | Mean | Std | Min | 25% | 50% | 75% | Max |
| Ascension | 69 | 0.73 | 0.14 | 0.42 | 0.64 | 0.75 | 0.85 | 0.92 |
| Namibe | 133 | 0.86 | 0.07 | 0.70 | 0.82 | 0.88 | 0.92 | 0.95 |
| 4STAR | 122 | 0.95 | 0.05 | 0.68 | 0.93 | 0.97 | 0.99 | 0.99 |

| (b) TC AOD (FT AOD) 532 nm | | | | | | | | |
|---|---|---|---|---|---|---|---|---|
| Site Name | Count | Mean | Std | Min | 25% | 50% | 75% | Max |
| Ascension | 69 | 0.31 | 0.15 | 0.10 | 0.18 | 0.28 | 0.40 | 0.88 |
|  |  | (0.23) | (0.15) | (0.08) | (0.10) | (0.18) | (0.33) | (0.81) |
| Namibe | 133 | 0.88 | 0.28 | 0.47 | 0.69 | 0.81 | 1.04 | 1.74 |
|  |  | (0.76) | (0.26) | (0.39) | (0.54) | (0.69) | (0.91) | (1.58) |
| 4STAR | 255 | 0.36 | 0.15 | 0.14 | 0.24 | 0.31 | 0.43 | 0.85 |
|  |  | (0.35) | (0.15) | (0.13) | (0.23) | (0.30) | (0.42) | (0.84) |

| (c) TC EAE (FT EAE) 440-870 nm | | | | | | | | |
|---|---|---|---|---|---|---|---|---|
| Site Name | Count | Mean | Std | Min | 25% | 50% | 75% | Max |
| Ascension | 69 | 0.96 | 0.27 | 0.28 | 0.74 | 0.96 | 1.18 | 1.52 |
|  |  | (0.97) | (0.28) | (0.28) | (0.75) | (0.97) | (1.20) | (1.54) |
| Namibe | 133 | 1.54 | 0.15 | 1.01 | 1.47 | 1.56 | 1.64 | 1.82 |
|  |  | (1.55) | (0.15) | (1.01) | (1.47) | (1.57) | (1.65) | (1.83) |
| 4STAR | 255 | 1.69 | 0.15 | 0.86 | 1.63 | 1.71 | 1.78 | 2.08 |
|  |  | (1.70) | (0.15) | (0.86) | (1.63) | (1.71) | (1.78) | (2.08) |

475

### 3.3.2 Free Tropospheric Extinction Ångstrom Exponent

The FT EAE values observed from 4STAR range between approximately 1.0 and 2.1, averaging 1.7, consistent with findings from Leblanc et al. (2020), that reported minimal spatial dependence of above-cloud EAE in the SEA. At Namibe, FT EAE ranges from 1.0 – 1.82 with mean of about 1.55.
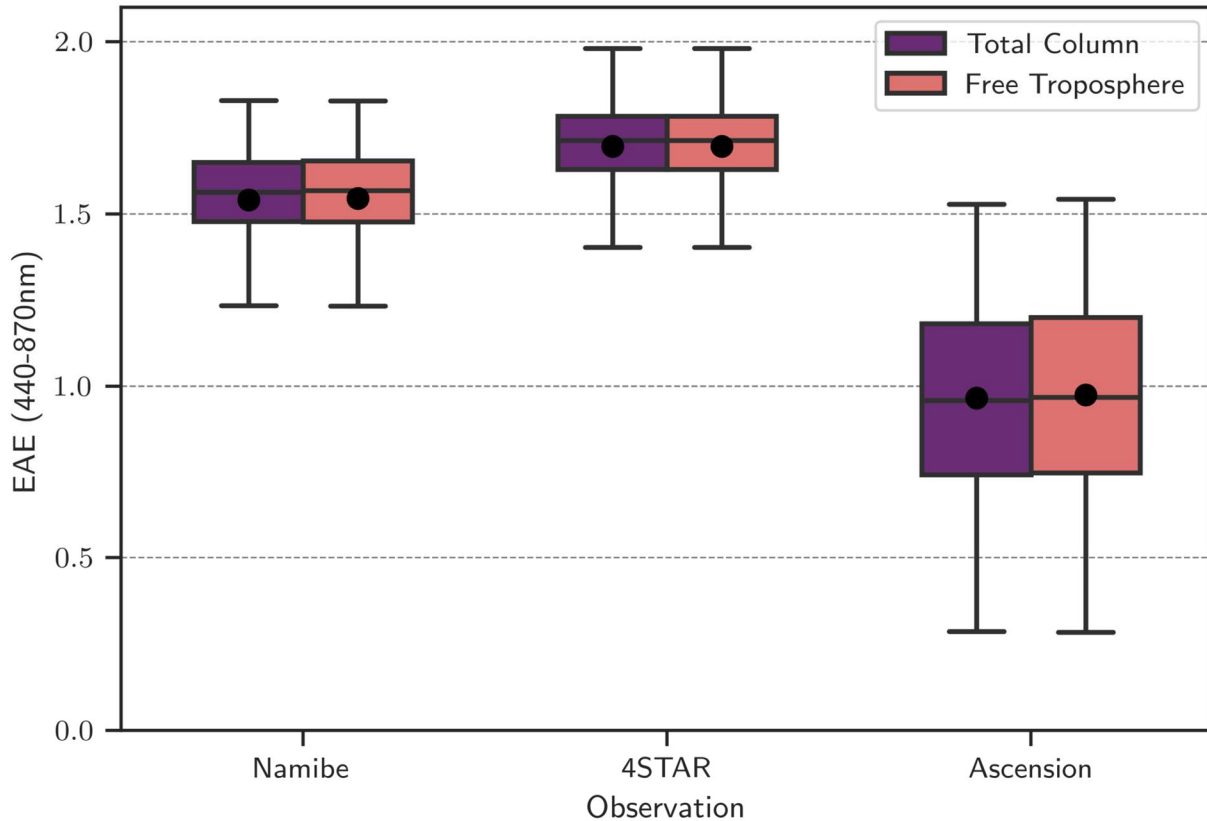
**Figure 9: Same as Figure 8 but for EAE (440-870 nm)**

At Ascension Island, the FT EAE ranges from 0.28 to 1.5 with a mean of approximately 1.0, indicating a variety of particle sizes. The EAE distribution within the FT mirrors the EAE values obtained from the TC, suggesting that the particles' intensive properties remain largely unchanged after isolating MBL contributions. Typically, TC AOD at Ascension that includes the other aerosol contribution would be expected to result in a lower EAE value than the FT AOD-derived value of EAE due to the presence of sea salt aerosols and dimethyl sulfide (DMS) in the maritime environment (Smirnov et al., 2002). However, the lower FT EAE values at Ascension Island suggest there is a source of advected coarse particles in the FT, especially for cases with FT EAE as low as 0.5 shown in Fig. 9. The FT EAE values from 4STAR in the ORACLES campaign region primarily reflect the characteristics of BBA, with mean EAE

values greater than 1.2 (Table 3), consistent with previous studies in the region (Pistone et al., 2019; Leblanc et al., 2020).

### 3.3.3 Free Tropospheric Single Scattering Albedo

Figure 10 shows the distribution of SSA, EAE and aerosol age in the free troposphere by observation site. Over the SEA, the FT SSA differs from that of the TC SSA (shown in Figure 4). At Namibe, the mean FT SSA is 0.85, from a range of 0.79 – 0.94. 4STAR observations show FT SSA values between 0.67 - 0.96, with a mean of 0.86. At Ascension Island, the FT SSA ranged from 0.60 - 0.98, with mean of 0.82 (Table 4). These values of FT SSA are lower than TC SSA due to exclusion of the BL portion of the TC, which may include other non-BBA aerosols with higher SSA. This difference between FT SSA and TC SSA over the SEA is further discussed in section 3.4. Given that there was no vertical partitioning in the source region since BBA dominates the full column, the FT SSA and TC SSA are equal.
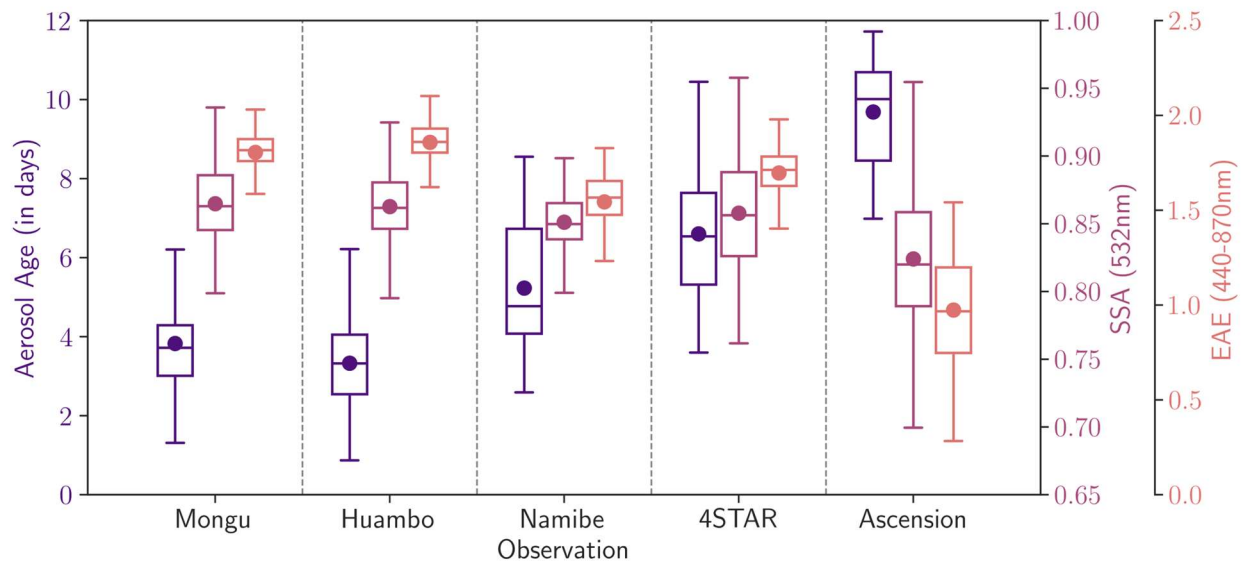
**Figure 10: Same as in Figure 4, but for the free troposphere (FT).**

**Table 4: Summary statistics of TC and FT (in parentheses) aerosol age (a), SSA (b) and EAE (c) based on observations site.**

**a.  Result Age**

| Site Name | Count | Mean | Std | Min | 25% | 50% | 75% | Max |
|---|---|---|---|---|---|---|---|---|
| Ascension | 69 | 9.77 | 1.16 | 7.77 | 8.99 | 9.97 | 10.7 | 11.73 |
| | | (9.68) | (1.32) | (6.98) | (8.45) | (10.02) | (10.69) | (11.73) |
| Namibe | 133 | 5.82 | 1.49 | 2.82 | 5.00 | 5.59 | 7.25 | 9.05 |
| | | (5.23) | (1.55) | (2.59) | (4.08) | (4.78) | (6.73) | (8.55) |
| Huambo | 336 | 3.33 | 1.10 | 0.87 | 2.54 | 3.32 | 4.05 | 6.80 |
| Mongu | 355 | 3.83 | 1.25 | 1.09 | 3.01 | 3.72 | 4.29 | 7.55 |
| 4STAR | 255 | 6.69 | 1.76 | 3.60 | 5.37 | 6.58 | 7.96 | 11.56 |
| | | (6.60) | (1.72) | (3.60) | (5.32) | (6.54) | (7.64) | (11.78) |

510

**b.  Single Scattering Albedo (SSA 532 nm)**

| Site Name | Count | Mean | Std | Min | 25% | 50% | 75% | Max |
|---|---|---|---|---|---|---|---|---|
| Ascension | 69 | 0.87 | 0.04 | 0.78 | 0.85 | 0.87 | 0.90 | 0.99 |
| | | (0.82) | (0.07) | (0.60) | (0.79) | (0.82) | (0.86) | (0.98) |
| Namibe | 133 | 0.87 | 0.02 | 0.83 | 0.86 | 0.87 | 0.88 | 0.95 |
| | | (0.85) | (0.02) | (0.79) | (0.84) | (0.85) | (0.86) | (0.94) |
| Huambo | 336 | 0.86 | 0.02 | 0.78 | 0.85 | 0.86 | 0.88 | 0.92 |
| Mongu | 355 | 0.86 | 0.03 | 0.77 | 0.84 | 0.86 | 0.89 | 0.97 |
| 4STAR | 255 | 0.86 | 0.04 | 0.67 | 0.83 | 0.85 | 0.89 | 0.96 |
| | | (0.86) | (0.05) | (0.67) | (0.82) | (0.85) | (0.88) | (0.96) |

**c.  Extinction Angstrom Exponent (EAE 440-870 nm)**

| Site Name | Count | Mean | Std | Min | 25% | 50% | 75% | Max |
|---|---|---|---|---|---|---|---|---|
| Ascension | 69 | 0.96 | 0.27 | 0.28 | 0.74 | 0.96 | 1.18 | 1.52 |
| | | (0.97) | (0.28) | (0.28) | (0.75) | (0.97) | (1.20) | (1.54) |
| Namibe | 133 | 1.54 | 0.15 | 1.01 | 1.47 | 1.56 | 1.64 | 1.82 |
| | | (1.55) | (0.15) | (1.01) | (1.47) | (1.57) | (1.65) | (1.83) |
| Huambo | 336 | 1.86 | 0.11 | 0.95 | 1.80 | 1.86 | 1.93 | 2.10 |
| Mongu | 355 | 1.81 | 0.11 | 1.33 | 1.76 | 1.81 | 1.87 | 2.05 |
| 4STAR | 255 | 1.69 | 0.15 | 0.86 | 1.63 | 1.71 | 1.78 | 2.08 |
| | | (1.70) | (0.15) | (0.86) | (1.63) | (1.71) | (1.78) | (2.08) |

### 3.4 Evolution of BBA SSA with age in the free troposphere

To further filter out larger particles within the free troposphere, particularly over Ascension Island, we applied a threshold of EAE ≥ 1.2 to the FT dataset, allowing us to focus our analysis on the temporal evolution of FT SSA during BBA-laden episodes. Our findings in Fig. 11 show a progressive increase in mean FT SSA from 0.84 to 0.87 as the aerosols age from 0 to 8 days. After 8 days, FT SSA decreases from 0.87, reaching 0.84 after approximately 12 days of transport. This trend in the mean FT SSA across age bins, summarized in Table 5, begins at 0.84 (0-2 days), increases to 0.857 (2-4 days), 0.862 (4-6 days), and peaks at 0.871 (6-8 days), before declining to 0.84 (8-10 days) and 0.845 (10-12 days). However, it is important to note the higher uncertainty in FT SSA for the 10-12 day age bin due to the reduced sample size following the EAE filtering (Table 5). We analyzed the contribution of FT SSA from each campaign month to the age bins after filtering (see Table S1 and S2).
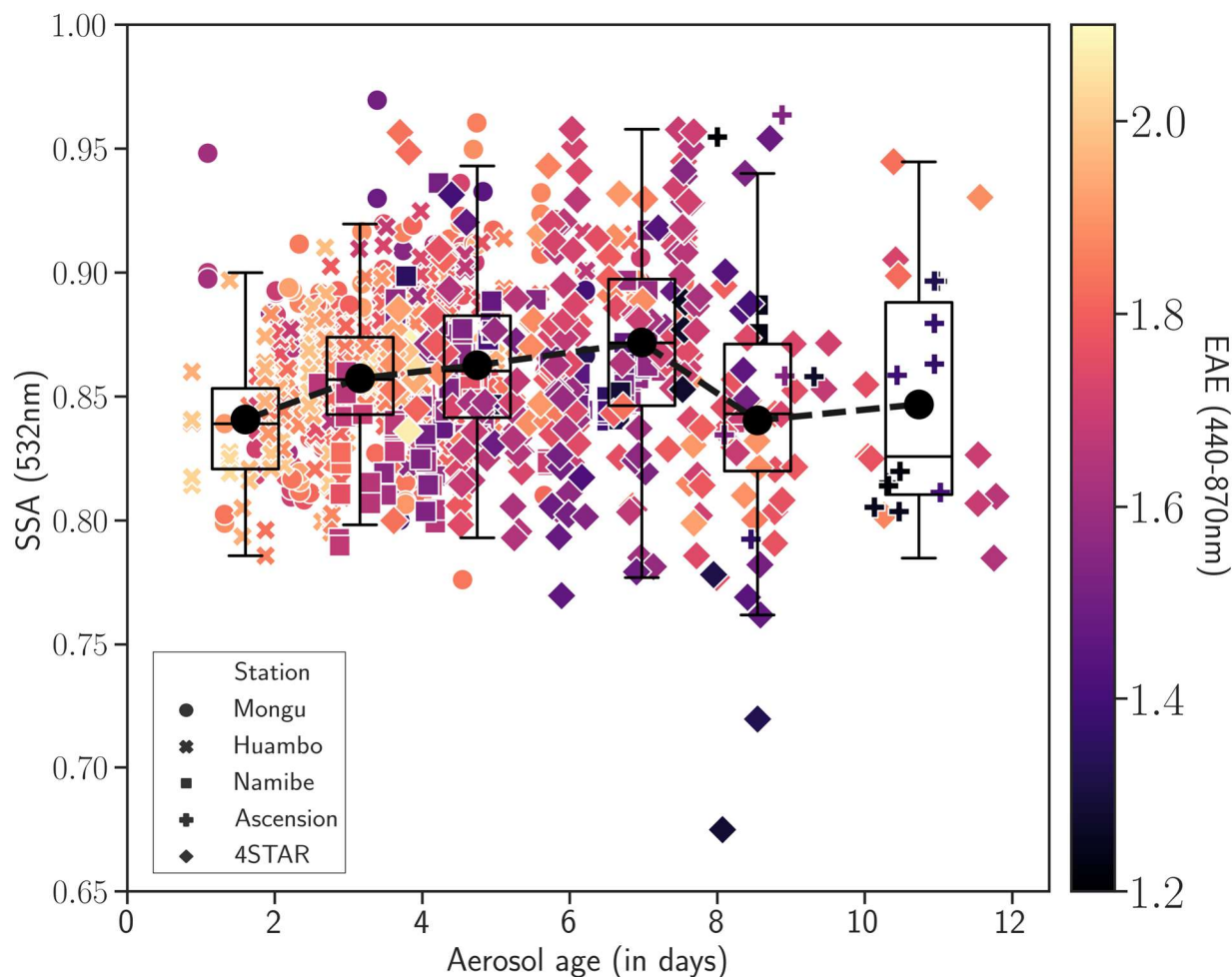
**Figure 11: Evolution of FT SSA as a function of aerosol age for the optimal threshold (EAE ≥ 1.2). Scatterplot shows the relationship between SSA, EAE and aerosol age for each observation. The box-whisker plots illustrate the distribution of SSA for the categorized aerosol age bins: [0-2], [2-4], [4-6], [6-8], [8-10], [10-12], showing the 10th (lower whisker), 25th**

**(lower box), 50th (median), 75th (upper box), and 90th (upper whisker) percentiles. The mean FT SSA for each age bin is represented in the black circles.**

530    The analysis showed that for October (2018), there are no observations in the 10-12 day bin and only (3) data points in the 8-10 day bin. In the 8-10 day bin, retrievals are nearly evenly distributed between August (2017) and September (2016), while in the 10-12 day bin, the ratio of September to August retrievals is approximately 3:1. The total number (3) of observations from October (2018) in the 8-10 day bin (3) and 10-12 day bin (0) represent less than 2% of total observations (229) for that year. Meanwhile, the contribution (27) from August (2017) and (42) from

535    September (2016) represent about 5% and 16% of the total observations (556 and 258, respectively) for the years. This distribution of observations in the 8-10 and 10-12 day bins suggests that the decrease in SSA observed for older aerosol plumes is not due to an overrepresentation of August data, which climatological studies suggest exhibit lower SSA due to their emissions earlier in the burning season. However, other factors, rather than the timing of the emission, drive the observed SSA change in aged plumes.

540    The maximum value of mean FT SSA at 6-8 days shows that the BBA absorptivity decreases as the aerosol ages from emission to about 6-8 days. After 6-8 days, the FT SSA decreases, indicating that older BBA are more efficient at absorbing solar radiation. This evolution of FT SSA supports the observations from previous studies where it was reported that the SSA initially increases within a few hours of emission and peaks on the fourth day before decreasing (Sedlacek et al., 2022). The results presented here also support the findings from Dobracki et al. (2023)

545    who showed that in the ORACLES region, SSA decreases as aerosols age because of a reduction in organic aerosol mass concentrations.

**Table 5: Summary statistics of TC SSA and FT SSA (in parentheses) for each age group at (EAE ≥ 1.2).**

| Age Group | Count | Mean | Std | Min | 25% | 50% | 75% | Max | SE |
|---|---|---|---|---|---|---|---|---|---|
| 0-2 | 47 | 0.841 | 0.03 | 0.785 | 0.820 | 0.840 | 0.853 | 0.948 | 0.004 |
|  | (47) | (0.84) | (0.03) | (0.785) | (0.820) | (0.840) | (0.853) | (0.948) | (0.004) |
| 2-4 | 425 | 0.859 | 0.02 | 0.795 | 0.845 | 0.859 | 0.874 | 0.960 | 0.001 |
|  | (430) | (0.857) | (0.03) | (0.790) | (0.843) | (0.857) | (0.874) | (0.96) | (0.001) |
| 4-6 | 319 | 0.868 | 0.03 | 0.776 | 0.847 | 0.865 | 0.887 | 0.960 | 0.001 |
|  | (327) | (0.862) | (0.03) | (0.769) | (0.841) | (0.860) | (0.882) | (0.960) | (0.001) |
| 6-8 | 169 | 0.871 | 0.04 | 0.778 | 0.847 | 0.873 | 0.895 | 0.958 | 0.003 |
|  | (167) | (0.871) | (0.04) | (0.777) | (0.846) | (0.871) | (0.897) | (0.958) | (0.003) |
| 8-10 | 64 | 0.861 | 0.05 | 0.675 | 0.829 | 0.860 | 0.896 | 0.970 | 0.007 |
|  | (49) | (0.840) | (0.05) | (0.675) | (0.820) | (0.843) | (0.871) | (0.963) | (0.008) |
| 10-12 | 16 | 0.858 | 0.04 | 0.802 | 0.827 | 0.843 | 0.901 | 0.944 | 0.011 |
|  | (23) | (0.845) | (0.04) | (0.785) | (0.810) | (0.825) | (0.890) | (0.944) | (0.009) |

We examined the mean FT SSA against the mean TC SSA at the established optimal EAE threshold (Fig.

550    12) to gain a clearer understanding of the evolution of SSA shown in Fig. 11 and to highlight the significance of

employing the combination of the model-based vertical extinction separation with an EAE filter. The results demonstrate that FT SSA decreases by more than 2% for BBA aged beyond 8 days. This decrease in the mean FT SSA compared to TC SSA suggests that by combining the two methods described in section 2.7, we are able to achieve our desired isolation of fine, BBA particles in the FT from the contribution of larger (EAE < 1.2), non-absorbing aerosols. Applying the EAE filtering solely to the TC data removed larger particles but did not account for other less absorbing fine particles, from mixing of BBA with marine aerosols with the boundary layer (Dang et al., 2022), or non-absorbing fine-mode marine aerosols (Fitzgerald, 1991). However, the application of the EAE filtering to the FT data after partitioning efficiently isolate all non-BBA particles. Overall, the combined use of both techniques, reveals a distinct evolution pattern of BBA in the FT. To examine the sensitivity of our assumption that $SSA_{BL} = 1$, we tested alternative $SSA_{BL}$ values to account for varying degrees of absorption within the BL. The results showed an evolution of FT SSA similar to that in Figure 12, with a decrease in the mean FT SSA after 8 days (supplemental Figure S6).

The changes in SSA presented in this study are primarily associated with chemical and physical processes in the atmosphere (Dobracki et al., 2023). Fresh aerosols over the continent exhibit a low SSA, which we attribute to a high proportion of rBC compared to other aerosol components. This interpretation agrees with previous findings further offshore (Denjean et al., 2020b; Wu et al., 2020; Dobracki et al., 2023) and is characteristic of emissions from flaming grassland fires. As these aerosols age in the atmosphere, they accumulate an organic coating, a process that begins rapidly within hours and continues for the first few days (Hodshire et al., 2019; Sedlacek et al., 2022), increasing the contribution of OA to the total mass of the aging particles. Unlike field measurements over the Atlantic Ocean that are relevant for more aged aerosols, our results show a progressive increase in SSA during the first 6 days of aging. After 6-8 days, however, the SSA starts to decrease, consistent with in-situ observations over the maritime atmosphere. We hypothesize that this decrease in SSA is due to increased absorption per particle from lensing effects, consistent with Taylor et al. (2020). Moreover, heterogeneous oxidation may drive the repartition of aerosol mass back to the gas phase, reducing the overall OA:BC mass ratio. In addition to compositional changes driven by the accumulation and/or evaporation of organic coatings, there is likely a shift in fine-mode particle size, potentially resulting from the same chemical and physical processes that also influence the optical properties.
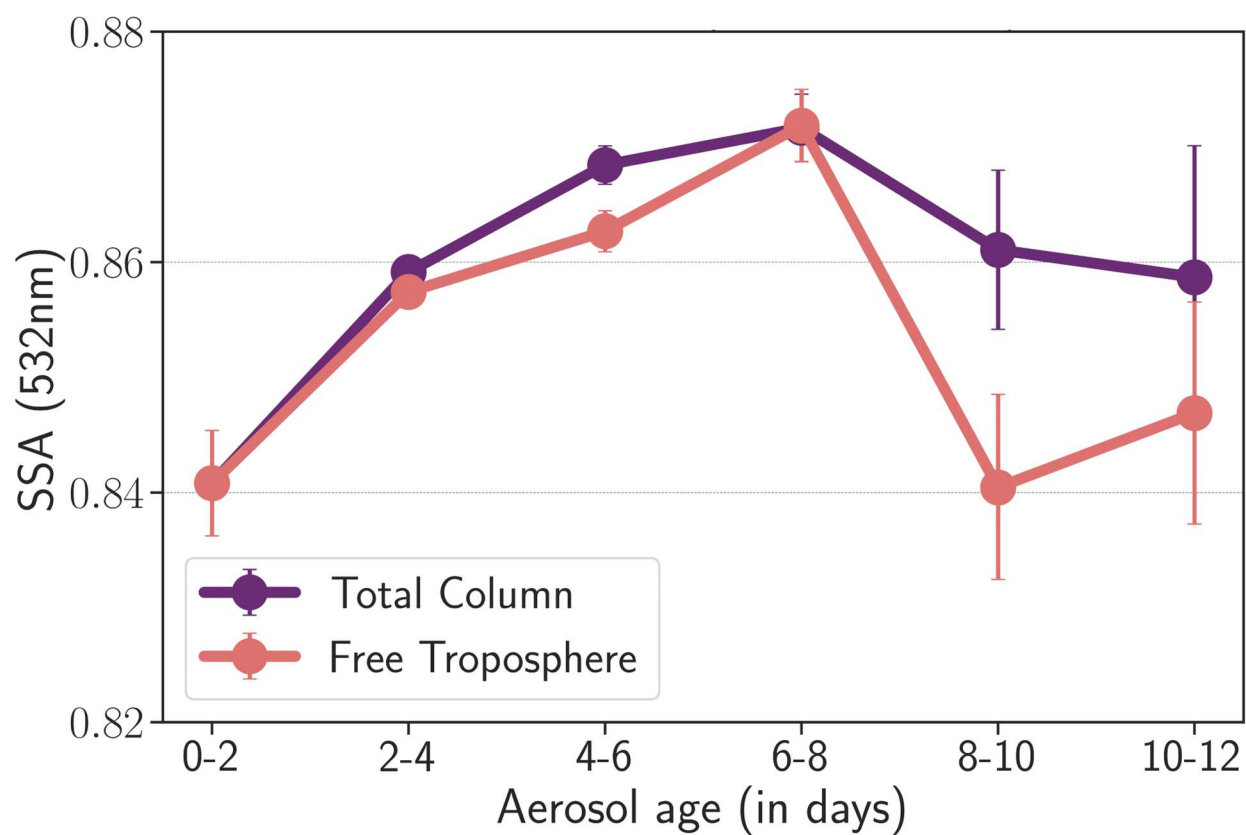
**Figure 12: Comparison between evolution of TC SSA and evolution of FT SSA for all the aerosol age bin at the optimal threshold (EAE ≥ 1.2). Error bars represent the standard error of the mean.**

### 4 Conclusions

We introduce a novel approach to investigate the evolution of optical properties of BBA during long-range transport from continental southern Africa to the SEA region. This approach integrates ground-based and airborne remote sensing measurements from AERONET and 4STAR, collected during the three ORACLES deployments, with model output from two WRF configurations: WRF-CAM5 and WRF-AAM, to extend the scope for studying aerosol evolution. Our analysis primarily focuses on examining the variations in observed SSA and AE in relation to the modeled age of the aerosols. This work is unique and builds upon the previous research over the SEA by including AERONET observations over land which allows for a more spatially extensive study of BBA evolution than those prior.

The WRF-AAM model, utilizing CO tracers, provided estimates of the aerosol age (defined as time elapsed since emission). We were able to assess how BBA optical properties evolved during long-range transport over the SEA by tracking the CO tracers in the model for a period of 2 weeks. Our result showed a longitudinal variation in SSA, that corresponds with the model-derived aerosol age and aligns with the transport pathway from the continent. The results revealed that SSA generally increased as BBA were transported away from the emission source, with lower SSA values measured at the Mongu and Huambo sites than those measured at the coastal Namibe site.

Throughout 2016, 2017, and 2018, there was a clear trend in mean SSA values, generally increasing with distance from the emission source while over land, with low values recorded at Mongu and Huambo, and the highest observed near the central African coast.

We next applied a model-based vertical separation and AE-based threshold to focus our analysis on the upper-level BBA observations over the SEA. Our analysis showed a distinct temporal trend in FT SSA, where mean FT SSA values initially increased from 0.84 to 0.87 during the first 7 days following emission, followed by a decline back to 0.84 after about 12 days. This implies that the observed aerosol aging led to a 0.03 change in SSA, a trend consistent with in-situ measurements reported during the ORACLES campaign by Sedlacek et al. (2022) and Dobracki et al. (2023). In Dobracki et al. (2023), a similar SSA change of approximately 0.06 was observed following a concomitant reduction in OA:BC mass ratio. Given that a variation of ±0.03 in SSA can result in a difference of up to ~20 Wm-2 in local direct radiative effect (Wilcox, 2012), the observed SSA changes in our analysis can have substantial effects on Earth's radiative budget, particularly in the SEA, especially considering the influence of BBA above clouds on the sign and magnitude of TOA forcing over dark ocean surface, as noted by Keil and Haywood (2003). To our knowledge, this study is the first to use remote sensing observations to document changes in BBA properties during long-range transport and associated aging.

We conclude from our analysis that BBA undergo variations in their optical properties that have important implications for the radiation balance. Upon emission, BBA are characterized by low SSA values (high absorptivity), and elevated AE values, indicating the prevalence of small sized particles. During initial stages of transport, BBA SSA increases, signifying a reduction absorptivity, accompanied by a decrease in AE, indicative of particle growth. However, there is a subsequent decrease in SSA (increase in absorptivity) as BBA continue to age during extended transport. This evolution is driven by atmospheric processes. Dobracki et al. (2023) attributed these changes in SSA to various chemical and physical transformation of BBA in the atmosphere.

These results, in agreement with the findings of Dobracki et al. (2023) and Sedlacek et al. (2022), emphasize the continuous evolution of BBA optical properties, influenced by changes in their chemical and microphysical properties. Accurately capturing these evolving properties throughout their lifecycle represents the next step for improving model fidelity and predictive capability. To the best of our knowledge, this study is among the first efforts to investigate BBA evolution over an extended temporal scale, spanning weeks, using columnar observations from remote sensing.

The data analysis techniques and findings from this study contribute to a greater understanding of how BBA optical properties change and the radiative effects associated with those changes. This research also provides further insight into the spatial and temporal evolution of BBA. More importantly, the changes in BBA optical properties associated with aging documented here and elsewhere will need to be incorporated into ESMs to accurately represent BBA aerosol properties and effects, and to properly predict future changes in BBA climatic impacts.

**Data Availability:**

The NASA P-3 aircraft data was published by ORACLES Science Team (2021) and can be accessed at these links:

630    ORACLES 2016: https://doi.org/10.5067/Suborbital/ORACLES/P3/2016_V3;

ORACLES 2017: https://doi.org/10.5067/Suborbital/ORACLES/P3/2017_V3;

ORACLES 2018: https://doi.org/10.5067/Suborbital/ORACLES/P3/2018_V3;

AERONET inversion products are available at https://aeronet.gsfc.nasa.gov/

**Author Contributions**

635    This study was conceptualized by JR. JR, CJF and AAF formulated the methodology. PES and CH ran the WRF simulations and provided model output. KP, SEL, MSR operated the 4STAR instrument aboard the P-3 aircraft and processed the 4STAR data. LM contributed to the processing of 4STAR retrievals. AAF organized all datasets, performed analyses, and visualized the results. PG and EL are the PIs for the AERONET network. JR and PZ led efforts to acquire funding and were the PIs for the ORACLES mission. AAF wrote the draft with contributions from

640    all authors.

**Competing Interests**

At least one of the (co-)authors is a member of the editorial board of Atmospheric Chemistry and Physics.

**Acknowledgements**

645    Portions of the computational work for this paper were supported by and conducted using resources at the University of Oklahoma (OU) Supercomputing Center for Education & Research (OSCER). We extend our gratitude to the entire NASA ORACLES team for their successful deployment. Our thanks also go to the site PIs and managers for the AERONET stations at Mongu, Huambo, Namibe and Ascension Island. Data analysis and visualization were carried out using open-source libraries in MATLAB and Python.

**650    Financial Support**

This research has been supported by the University of Oklahoma (OU) start-up package (grant no. 122007900). The ORACLES field campaign was funded through the NASA Earth Venture Suborbital-2 program (grant no. NNH13ZDA001N-EVS2). PZ acknowledges funding support from DOE ASR award DE-SC0021250.

**References**

655    Abel, S. J., Haywood, J. M., Highwood, E. J., Li, J., and Buseck, P. R.: Evolution of biomass burning aerosol properties from an agricultural fire in southern Africa, Geophysical Research Letters, 30, https://doi.org/10.1029/2003GL017342, 2003.

Ackerman, A. S., Toon, O. B., Taylor, J. P., Johnson, D. W., Hobbs, P. V., and Ferek, R. J.: Effects of Aerosols on Cloud Albedo: Evaluation of Twomey's Parameterization of Cloud Susceptibility 660    Using Measurements of Ship Tracks, Journal of the Atmospheric Sciences, 57, 2684-2695, 10.1175/1520-0469(2000)057<2684:Eoaoca>2.0.Co;2, 2000.

Adebiyi, A. A. and Zuidema, P.: The role of the southern African easterly jet in modifying the southeast Atlantic aerosol and cloud environments, Quarterly Journal of the Royal Meteorological Society, 142, 1574-1589, https://doi.org/10.1002/qj.2765, 2016.

665    Adebiyi, A. A., Zuidema, P., and Abel, S. J.: The Convolution of Dynamics and Moisture with the Presence of Shortwave Absorbing Aerosols over the Southeast Atlantic, Journal of Climate, 28, 1997-2024, 10.1175/jcli-d-14-00352.1, 2015.

Aladodo, S. S., Akoshile, C. O., Ajibola, T. B., Sani, M., Iborida, O. A., and Fakoya, A. A.: Seasonal Tropospheric Aerosol Classification Using AERONET Spectral Absorption Properties in African 670    Locations, Aerosol Science and Engineering, 6, 246-266, 10.1007/s41810-022-00140-x, 2022.

Albrecht, B. A.: Aerosols, Cloud Microphysics, and Fractional Cloudiness, Science, 245, 1227-1230, doi:10.1126/science.245.4923.1227, 1989.

Alexander, D. T. L., Crozier, P. A., and Anderson, J. R.: Brown Carbon Spheres in East Asian Outflow and Their Optical Properties, Science, 321, 833-836, doi:10.1126/science.1155296, 2008.

675    Andreae, M. O. and Gelencsér, A.: Black carbon or brown carbon? The nature of light-absorbing carbonaceous aerosols, Atmos. Chem. Phys., 6, 3131-3148, 10.5194/acp-6-3131-2006, 2006.

Andreae, M. O. and Rosenfeld, D.: Aerosol–cloud–precipitation interactions. Part 1. The nature and sources of cloud-active aerosols, Earth-Science Reviews, 89, 13-41, https://doi.org/10.1016/j.earscirev.2008.03.001, 2008.

680    Baars, H., Radenz, M., Floutsi, A. A., Engelmann, R., Althausen, D., Heese, B., Ansmann, A., Flament, T., Dabas, A., Trapon, D., Reitebuch, O., Bley, S., and Wandinger, U.: Californian Wildfire Smoke Over Europe: A First Example of the Aerosol Observing Capabilities of Aeolus Compared to Ground-Based Lidar, Geophysical Research Letters, 48, e2020GL092194, https://doi.org/10.1029/2020GL092194, 2021.

685    Bellouin, N., Quaas, J., Gryspeerdt, E., Kinne, S., Stier, P., Watson-Parris, D., Boucher, O., Carslaw, K. S., Christensen, M., Daniau, A.-L., Dufresne, J.-L., Feingold, G., Fiedler, S., Forster, P., Gettelman, A., Haywood, J. M., Lohmann, U., Malavelle, F., Mauritsen, T., McCoy, D. T., Myhre, G.,

Mülmenstädt, J., Neubauer, D., Possner, A., Rugenstein, M., Sato, Y., Schulz, M., Schwartz, S. E., Sourdeval, O., Storelvmo, T., Toll, V., Winker, D., and Stevens, B.: Bounding Global Aerosol Radiative Forcing of Climate Change, Reviews of Geophysics, 58, e2019RG000660, https://doi.org/10.1029/2019RG000660, 2020.

Bergstrom, R. W., Pilewskie, P., Russell, P. B., Redemann, J., Bond, T. C., Quinn, P. K., and Sierau, B.: Spectral absorption properties of atmospheric aerosols, Atmos. Chem. Phys., 7, 5937-5943, 10.5194/acp-7-5937-2007, 2007.

Bond, T. C., Habib, G., and Bergstrom, R. W.: Limitations in the enhancement of visible light absorption due to mixing state, Journal of Geophysical Research: Atmospheres, 111, 2006.

Bond, T. C., Streets, D. G., Yarber, K. F., Nelson, S. M., Woo, J.-H., and Klimont, Z.: A technology-based global inventory of black and organic carbon emissions from combustion, Journal of Geophysical Research: Atmospheres, 109, https://doi.org/10.1029/2003JD003697, 2004.

Bond, T. C., Doherty, S. J., Fahey, D. W., Forster, P. M., Berntsen, T., DeAngelo, B. J., Flanner, M. G., Ghan, S., Kärcher, B., Koch, D., Kinne, S., Kondo, Y., Quinn, P. K., Sarofim, M. C., Schultz, M. G., Schulz, M., Venkataraman, C., Zhang, H., Zhang, S., Bellouin, N., Guttikunda, S. K., Hopke, P. K., Jacobson, M. Z., Kaiser, J. W., Klimont, Z., Lohmann, U., Schwarz, J. P., Shindell, D., Storelvmo, T., Warren, S. G., and Zender, C. S.: Bounding the role of black carbon in the climate system: A scientific assessment, Journal of Geophysical Research: Atmospheres, 118, 5380-5552, 10.1002/jgrd.50171, 2013.

Boucher, O.: Atmospheric Aerosols, in: Atmospheric Aerosols: Properties and Climate Impacts, Springer Netherlands, Dordrecht, 9-24, 10.1007/978-94-017-9649-1_2, 2015.

Boucher, O., Randall, D., Artaxo, P., Bretherton, C., Feingold, G., Forster, P., Kerminen, V.-M., Kondo, Y., Liao, H., Lohmann, U., Rasch, P., Satheesh, S., Sherwood, S., Stevens, B., and Zhang, X.: Clouds and Aerosols, in: Climate Change 2013: The Physical Science Basis. Contribution of Working Group I to the Fifth Assessment Report of the Intergovernmental Panel on Climate Change, edited by: Change, I. P. o. C., Cambridge University Press, 571-892, 10.1017/CBO9781107415324.016., 2013.

Bowman, D. M. J. S., Balch, J. K., Artaxo, P., Bond, W. J., Carlson, J. M., Cochrane, M. A., D'Antonio, C. M., DeFries, R. S., Doyle, J. C., Harrison, S. P., Johnston, F. H., Keeley, J. E., Krawchuk, M. A., Kull, C. A., Marston, J. B., Moritz, M. A., Prentice, I. C., Roos, C. I., Scott, A. C., Swetnam, T. W., van der Werf, G. R., and Pyne, S. J.: Fire in the Earth System, Science, 324, 481-484, doi:10.1126/science.1163886, 2009.

Brown, H., Liu, X., Pokhrel, R., Murphy, S., Lu, Z., Saleh, R., Mielonen, T., Kokkola, H., Bergman, T., Myhre, G., Skeie, R. B., Watson-Paris, D., Stier, P., Johnson, B., Bellouin, N., Schulz, M., Vakkari,

V., Beukes, J. P., van Zyl, P. G., Liu, S., and Chand, D.: Biomass burning aerosols in most climate models are too absorbing, Nat Commun, 12, 277, 10.1038/s41467-020-20482-9, 2021.

Campbell, P., Zhang, Y., Wang, K., Leung, R., Fan, J., Zheng, B., Zhang, Q., and He, K.: Evaluation of a multi-scale WRF-CAM5 simulation during the 2010 East Asian Summer Monsoon, Atmospheric Environment, 169, 204-217, https://doi.org/10.1016/j.atmosenv.2017.09.008, 2017.

Chand, D., Wood, R., Anderson, T. L., Satheesh, S. K., and Charlson, R. J.: Satellite-derived direct radiative effect of aerosols dependent on cloud cover, Nature Geoscience, 2, 181-184, 10.1038/ngeo437, 2009.

Chang, I., Gao, L., Flynn, C. J., Shinozuka, Y., Doherty, S. J., Diamond, M. S., Longo, K. M., Ferrada, G. A., Carmichael, G. R., Castellanos, P., da Silva, A. M., Saide, P. E., Howes, C., Xue, Z., Mallet, M., Govindaraju, R., Wang, Q., Cheng, Y., Feng, Y., Burton, S. P., Ferrare, R. A., LeBlanc, S. E., Kacenelenbogen, M. S., Pistone, K., Segal-Rozenhaimer, M., Meyer, K. G., Ryoo, J. M., Pfister, L., Adebiyi, A. A., Wood, R., Zuidema, P., Christopher, S. A., and Redemann, J.: On the differences in the vertical distribution of modeled aerosol optical depth over the southeastern Atlantic, Atmos. Chem. Phys., 23, 4283-4309, 10.5194/acp-23-4283-2023, 2023.

Che, H., Stier, P., Gordon, H., Watson-Parris, D., and Deaconu, L.: Cloud adjustments dominate the overall negative aerosol radiative effects of biomass burning aerosols in UKESM1 climate model simulations over the south-eastern Atlantic, Atmos. Chem. Phys., 21, 17-33, 10.5194/acp-21-17-2021, 2021.

Chylek, P. and Wong, J.: Effect of absorbing aerosols on global radiation budget, Geophysical Research Letters, 22, 929-931, https://doi.org/10.1029/95GL00800, 1995.

Collier, S., Zhou, S., Onasch, T. B., Jaffe, D. A., Kleinman, L., Sedlacek, A. J., III, Briggs, N. L., Hee, J., Fortner, E., Shilling, J. E., Worsnop, D., Yokelson, R. J., Parworth, C., Ge, X., Xu, J., Butterfield, Z., Chand, D., Dubey, M. K., Pekour, M. S., Springston, S., and Zhang, Q.: Regional Influence of Aerosol Emissions from Wildfires Driven by Combustion Efficiency: Insights from the BBOP Campaign, Environmental Science & Technology, 50, 8613-8622, 10.1021/acs.est.6b01617, 2016.

Dang, C., Segal-Rozenhaimer, M., Che, H., Zhang, L., Formenti, P., Taylor, J., Dobracki, A., Purdue, S., Wong, P. S., Nenes, A., Sedlacek Iii, A., Coe, H., Redemann, J., Zuidema, P., Howell, S., and Haywood, J.: Biomass burning and marine aerosol processing over the southeast Atlantic Ocean: a TEM single-particle analysis, Atmos. Chem. Phys., 22, 9389-9412, 10.5194/acp-22-9389-2022, 2022.

Darmenov, A. S. and da Silva, A.: The Quick Fire Emissions Dataset (QFED): Documentation of versions 2.1, 2.2 and 2.4, NASA, 2015.

755 de Graaf, M., Bellouin, N., Tilstra, L. G., Haywood, J., and Stammes, P.: Aerosol direct radiative effect of smoke over clouds over the southeast Atlantic Ocean from 2006 to 2009, Geophysical Research Letters, 41, 7723-7730, https://doi.org/10.1002/2014GL061103, 2014.

Dedrick, J. L., Russell, L. M., Sedlacek Iii, A. J., Kuang, C., Zawadowicz, M. A., and Lubin, D.: Aerosol-Correlated Cloud Activation for Clean Conditions in the Tropical Atlantic Boundary Layer During
760 LASIC, Geophysical Research Letters, 51, e2023GL105798, https://doi.org/10.1029/2023GL105798, 2024.

Denjean, C., Brito, J., Libois, Q., Mallet, M., Bourrianne, T., Burnet, F., Dupuy, R., Flamant, C., and Knippertz, P.: Unexpected Biomass Burning Aerosol Absorption Enhancement Explained by Black Carbon Mixing State, Geophysical Research Letters, 47, e2020GL089055,
765 https://doi.org/10.1029/2020GL089055, 2020b.

Denjean, C., Bourrianne, T., Burnet, F., Mallet, M., Maury, N., Colomb, A., Dominutti, P., Brito, J., Dupuy, R., Sellegri, K., Schwarzenboeck, A., Flamant, C., and Knippertz, P.: Overview of aerosol optical properties over southern West Africa from DACCIWA aircraft measurements, Atmos. Chem. Phys., 20, 4735-4756, 10.5194/acp-20-4735-2020, 2020a.

770 Diamond, M. S., Dobracki, A., Freitag, S., Small Griswold, J. D., Heikkila, A., Howell, S. G., Kacarab, M. E., Podolske, J. R., Saide, P. E., and Wood, R.: Time-dependent entrainment of smoke presents an observational challenge for assessing aerosol–cloud interactions over the southeast Atlantic Ocean, Atmos. Chem. Phys., 18, 14623-14636, 10.5194/acp-18-14623-2018, 2018.

Dobracki, A., Lewis, E. R., Sedlacek Iii, A. J., Tatro, T., Zawadowicz, M. A., and Zuidema, P.: Burning
775 conditions and transportation pathways determine biomass-burning aerosol properties in the Ascension Island marine boundary layer, Atmos. Chem. Phys., 25, 2333-2363, 10.5194/acp-25-2333-2025, 2025.

Dobracki, A., Zuidema, P., Howell, S. G., Saide, P., Freitag, S., Aiken, A. C., Burton, S. P., Sedlacek Iii, A. J., Redemann, J., and Wood, R.: An attribution of the low single-scattering albedo of biomass
780 burning aerosol over the southeastern Atlantic, Atmos. Chem. Phys., 23, 4775-4799, 10.5194/acp-23-4775-2023, 2023.

Doherty, S. J., Saide, P. E., Zuidema, P., Shinozuka, Y., Ferrada, G. A., Gordon, H., Mallet, M., Meyer, K., Painemal, D., Howell, S. G., Freitag, S., Dobracki, A., Podolske, J. R., Burton, S. P., Ferrare, R. A., Howes, C., Nabat, P., Carmichael, G. R., da Silva, A., Pistone, K., Chang, I., Gao, L., Wood,
785 R., and Redemann, J.: Modeled and observed properties related to the direct aerosol radiative effect of biomass burning aerosol over the southeastern Atlantic, Atmos. Chem. Phys., 22, 1-46, 10.5194/acp-22-1-2022, 2022.

Dubovik, O., Holben, B., Eck, T. F., Smirnov, A., Kaufman, Y. J., King, M. D., Tanré, D., and Slutsker, I.: Variability of Absorption and Optical Properties of Key Aerosol Types Observed in Worldwide Locations, Journal of the Atmospheric Sciences, 59, 590-608, 10.1175/1520-0469(2002)059<0590:Voaaop>2.0.Co;2, 2002.

Dunagan, S. E., Johnson, R., Zavaleta, J., Russell, P. B., Schmid, B., Flynn, C., Redemann, J., Shinozuka, Y., Livingston, J., and Segal-Rosenhaimer, M.: Spectrometer for Sky-Scanning Sun-Tracking Atmospheric Research (4STAR): Instrument Technology, Remote Sensing, 5, 3872-3895, 2013.

Eck, T. F., Holben, B. N., Reid, J. S., Dubovik, O., Smirnov, A., O'Neill, N. T., Slutsker, I., and Kinne, S.: Wavelength dependence of the optical depth of biomass burning, urban, and desert dust aerosols, Journal of Geophysical Research: Atmospheres, 104, 31333-31349, https://doi.org/10.1029/1999JD900923, 1999.

Eck, T. F., Holben, B. N., Ward, D. E., Mukelabai, M. M., Dubovik, O., Smirnov, A., Schafer, J. S., Hsu, N. C., Piketh, S. J., Queface, A., Roux, J. L., Swap, R. J., and Slutsker, I.: Variability of biomass burning aerosol optical characteristics in southern Africa during the SAFARI 2000 dry season campaign and a comparison of single scattering albedo estimates from radiometric measurements, Journal of Geophysical Research: Atmospheres, 108, https://doi.org/10.1029/2002JD002321, 2003.

Eck, T. F., Holben, B. N., Reid, J. S., Mukelabai, M. M., Piketh, S. J., Torres, O., Jethva, H. T., Hyer, E. J., Ward, D. E., Dubovik, O., Sinyuk, A., Schafer, J. S., Giles, D. M., Sorokin, M., Smirnov, A., and Slutsker, I.: A seasonal trend of single scattering albedo in southern African biomass-burning particles: Implications for satellite products and estimates of emissions for the world's largest biomass-burning source, Journal of Geophysical Research: Atmospheres, 118, 6414-6432, https://doi.org/10.1002/jgrd.50500, 2013.

Feng, X., Wang, J., Teng, S., Xu, X., Zhu, B., Wang, J., Zhu, X., Yurkin, M. A., and Liu, C.: Can light absorption of black carbon still be enhanced by mixing with absorbing materials?, Atmospheric Environment, 253, 118358, https://doi.org/10.1016/j.atmosenv.2021.118358, 2021.

Feng, Y., Ramanathan, V., and Kotamarthi, V. R.: Brown carbon: a significant atmospheric absorber of solar radiation?, Atmos. Chem. Phys., 13, 8607-8621, 10.5194/acp-13-8607-2013, 2013.

Fitzgerald, J. W.: Marine aerosols: A review, Atmospheric Environment. Part A. General Topics, 25, 533-545, https://doi.org/10.1016/0960-1686(91)90050-H, 1991.

Formenti, P., D'Anna, B., Flamant, C., Mallet, M., Piketh, S. J., Schepanski, K., Waquet, F., Auriol, F., Brogniez, G., Burnet, F., Chaboureau, J.-P., Chauvigné, A., Chazette, P., Denjean, C., Desboeufs, K., Doussin, J.-F., Elguindi, N., Feuerstein, S., Gaetani, M., Giorio, C., Klopper, D., Mallet, M. D., Nabat, P., Monod, A., Solmon, F., Namwoonde, A., Chikwililwa, C., Mushi, R., Welton, E. J., and

Holben, B.: The Aerosols, Radiation and Clouds in Southern Africa Field Campaign in Namibia: Overview, Illustrative Observations, and Way Forward, Bulletin of the American Meteorological Society, 100, 1277-1298, 10.1175/bams-d-17-0278.1, 2019.

825    Giles, D. M., Sinyuk, A., Sorokin, M. G., Schafer, J. S., Smirnov, A., Slutsker, I., Eck, T. F., Holben, B. N., Lewis, J. R., Campbell, J. R., Welton, E. J., Korkin, S. V., and Lyapustin, A. I.: Advancements in the Aerosol Robotic Network (AERONET) Version 3 database – automated near-real-time quality control algorithm with improved cloud screening for Sun photometer aerosol optical depth (AOD) measurements, Atmos. Meas. Tech., 12, 169-209, 10.5194/amt-12-169-2019, 2019.

830    Granier, C., Bessagnet, B., Bond, T., D'Angiola, A., Denier van der Gon, H., Frost, G. J., Heil, A., Kaiser, J. W., Kinne, S., Klimont, Z., Kloster, S., Lamarque, J.-F., Liousse, C., Masui, T., Meleux, F., Mieville, A., Ohara, T., Raut, J.-C., Riahi, K., Schultz, M. G., Smith, S. J., Thompson, A., van Aardenne, J., van der Werf, G. R., and van Vuuren, D. P.: Evolution of anthropogenic and biomass burning emissions of air pollutants at global and regional scales during the 1980–2010 period, 835      Climatic Change, 109, 163, 10.1007/s10584-011-0154-1, 2011.

Grell, G. A., Peckham, S. E., Schmitz, R., McKeen, S. A., Frost, G., Skamarock, W. C., and Eder, B.: Fully coupled "online" chemistry within the WRF model, Atmospheric Environment, 39, 6957-6975, https://doi.org/10.1016/j.atmosenv.2005.04.027, 2005.

Hansen, J., Sato, M., and Ruedy, R.: Radiative forcing and climate response, Journal of Geophysical 840      Research: Atmospheres, 102, 6831-6864, https://doi.org/10.1029/96JD03436, 1997.

Haywood, J. M. and Shine, K. P.: Multi-spectral calculations of the direct radiative forcing of tropospheric sulphate and soot aerosols using a column model, Quarterly Journal of the Royal Meteorological Society, 123, 1907-1930, https://doi.org/10.1002/qj.49712354307, 1997.

Haywood, J. M., Osborne, S. R., Francis, P. N., Keil, A., Formenti, P., Andreae, M. O., and Kaye, P. H.: 845      The mean physical and optical properties of regional haze dominated by biomass burning aerosol measured from the C-130 aircraft during SAFARI 2000, Journal of Geophysical Research: Atmospheres, 108, https://doi.org/10.1029/2002JD002226, 2003.

Haywood, J. M., Abel, S. J., Barrett, P. A., Bellouin, N., Blyth, A., Bower, K. N., Brooks, M., Carslaw, K., Che, H., Coe, H., Cotterell, M. I., Crawford, I., Cui, Z., Davies, N., Dingley, B., Field, P., Formenti, 850      P., Gordon, H., de Graaf, M., Herbert, R., Johnson, B., Jones, A. C., Langridge, J. M., Malavelle, F., Partridge, D. G., Peers, F., Redemann, J., Stier, P., Szpek, K., Taylor, J. W., Watson-Parris, D., Wood, R., Wu, H., and Zuidema, P.: The CLoud–Aerosol–Radiation Interaction and Forcing: Year 2017 (CLARIFY-2017) measurement campaign, Atmos. Chem. Phys., 21, 1049-1084, 10.5194/acp-21-1049-2021, 2021.

855    Hodshire, A. L., Akherati, A., Alvarado, M. J., Brown-Steiner, B., Jathar, S. H., Jimenez, J. L., Kreidenweis, S. M., Lonsdale, C. R., Onasch, T. B., Ortega, A. M., and Pierce, J. R.: Aging Effects on Biomass Burning Aerosol Mass and Composition: A Critical Review of Field and Laboratory Studies, Environmental Science & Technology, 53, 10007-10022, 10.1021/acs.est.9b02588, 2019.

Holanda, B. A., Pöhlker, M. L., Walter, D., Saturno, J., Sörgel, M., Ditas, J., Ditas, F., Schulz, C., Franco,
860    M. A., Wang, Q., Donth, T., Artaxo, P., Barbosa, H. M. J., Borrmann, S., Braga, R., Brito, J., Cheng, Y., Dollner, M., Kaiser, J. W., Klimach, T., Knote, C., Krüger, O. O., Fütterer, D., Lavrič, J. V., Ma, N., Machado, L. A. T., Ming, J., Morais, F. G., Paulsen, H., Sauer, D., Schlager, H., Schneider, J., Su, H., Weinzierl, B., Walser, A., Wendisch, M., Ziereis, H., Zöger, M., Pöschl, U., Andreae, M. O., and Pöhlker, C.: Influx of African biomass burning aerosol during the Amazonian
865    dry season through layered transatlantic transport of black carbon-rich smoke, Atmos. Chem. Phys., 20, 4757-4785, 10.5194/acp-20-4757-2020, 2020.

Holben, B. N., Eck, T. F., Slutsker, I., Tanré, D., Buis, J. P., Setzer, A., Vermote, E., Reagan, J. A., Kaufman, Y. J., Nakajima, T., Lavenu, F., Jankowiak, I., and Smirnov, A.: AERONET—A Federated Instrument Network and Data Archive for Aerosol Characterization, Remote Sensing of
870    Environment, 66, 1-16, https://doi.org/10.1016/S0034-4257(98)00031-5, 1998.

Hopkins, R. J., Lewis, K., Desyaterik, Y., Wang, Z., Tivanski, A. V., Arnott, W. P., Laskin, A., and Gilles, M. K.: Correlations between optical, chemical and physical properties of biomass burn aerosols, Geophysical Research Letters, 34, https://doi.org/10.1029/2007GL030502, 2007.

Howes, C., Saide, P. E., Coe, H., Dobracki, A., Freitag, S., Haywood, J. M., Howell, S. G., Gupta, S., Uin,
875    J., Kacarab, M., Kuang, C., Leung, L. R., Nenes, A., McFarquhar, G. M., Podolske, J., Redemann, J., Sedlacek, A. J., Thornhill, K. L., Wong, J. P. S., Wood, R., Wu, H., Zhang, Y., Zhang, J., and Zuidema, P.: Biomass-burning smoke's properties and its interactions with marine stratocumulus clouds in WRF-CAM5 and southeastern Atlantic field campaigns, Atmos. Chem. Phys., 23, 13911-13940, 10.5194/acp-23-13911-2023, 2023.

880    Jen, C. N., Hatch, L. E., Selimovic, V., Yokelson, R. J., Weber, R., Fernandez, A. E., Kreisberg, N. M., Barsanti, K. C., and Goldstein, A. H.: Speciated and total emission factors of particulate organics from burning western US wildland fuels and their dependence on combustion efficiency, Atmos. Chem. Phys., 19, 1013-1026, 10.5194/acp-19-1013-2019, 2019.

Jimenez, J. L., Canagaratna, M. R., Donahue, N. M., Prevot, A. S. H., Zhang, Q., Kroll, J. H., DeCarlo, P.
885    F., Allan, J. D., Coe, H., Ng, N. L., Aiken, A. C., Docherty, K. S., Ulbrich, I. M., Grieshop, A. P., Robinson, A. L., Duplissy, J., Smith, J. D., Wilson, K. R., Lanz, V. A., Hueglin, C., Sun, Y. L., Tian, J., Laaksonen, A., Raatikainen, T., Rautiainen, J., Vaattovaara, P., Ehn, M., Kulmala, M., Tomlinson, J. M., Collins, D. R., Cubison, M. J., E., Dunlea, J., Huffman, J. A., Onasch, T. B.,

Alfarra, M. R., Williams, P. I., Bower, K., Kondo, Y., Schneider, J., Drewnick, F., Borrmann, S.,
890     Weimer, S., Demerjian, K., Salcedo, D., Cottrell, L., Griffin, R., Takami, A., Miyoshi, T.,
Hatakeyama, S., Shimono, A., Sun, J. Y., Zhang, Y. M., Dzepina, K., Kimmel, J. R., Sueper, D.,
Jayne, J. T., Herndon, S. C., Trimborn, A. M., Williams, L. R., Wood, E. C., Middlebrook, A. M.,
Kolb, C. E., Baltensperger, U., and Worsnop, D. R.: Evolution of Organic Aerosols in the
Atmosphere, Science, 326, 1525-1529, doi:10.1126/science.1180353, 2009.

895 Jones, M. W., Abatzoglou, J. T., Veraverbeke, S., Andela, N., Lasslop, G., Forkel, M., Smith, A. J. P.,
Burton, C., Betts, R. A., van der Werf, G. R., Sitch, S., Canadell, J. G., Santín, C., Kolden, C.,
Doerr, S. H., and Le Quéré, C.: Global and Regional Trends and Drivers of Fire Under Climate
Change, Reviews of Geophysics, 60, e2020RG000726, https://doi.org/10.1029/2020RG000726,
2022.

900 Keil, A. and Haywood, J. M.: Solar radiative forcing by biomass burning aerosol particles during SAFARI
2000: A case study based on measured aerosol and cloud properties, Journal of Geophysical
Research: Atmospheres, 108, https://doi.org/10.1029/2002JD002315, 2003.

Keywood, M., Kanakidou, M., Stohl, A., Dentener, F., Grassi, G., Meyer, C. P., Torseth, K., Edwards, D.,
Thompson, A. M., Lohmann, U., and Burrows, J.: Fire in the Air: Biomass Burning Impacts in a
905     Changing Climate, Critical Reviews in Environmental Science and Technology, 43, 40-83,
10.1080/10643389.2011.604248, 2013.

Kleinman, L. I., Sedlacek Iii, A. J., Adachi, K., Buseck, P. R., Collier, S., Dubey, M. K., Hodshire, A. L.,
Lewis, E., Onasch, T. B., Pierce, J. R., Shilling, J., Springston, S. R., Wang, J., Zhang, Q., Zhou,
S., and Yokelson, R. J.: Rapid evolution of aerosol particles and their optical properties downwind
910     of wildfires in the western US, Atmos. Chem. Phys., 20, 13319-13341, 10.5194/acp-20-13319-
2020, 2020.

Koch, D. and Del Genio, A. D.: Black carbon semi-direct effects on cloud cover: review and synthesis,
Atmos. Chem. Phys., 10, 7685-7696, 10.5194/acp-10-7685-2010, 2010.

Konovalov, I. B., Golovushkin, N. A., Beekmann, M., and Andreae, M. O.: Insights into the aging of
915     biomass burning aerosol from satellite observations and 3D atmospheric modeling: evolution of
the aerosol optical properties in Siberian wildfire plumes, Atmos. Chem. Phys., 21, 357-392,
10.5194/acp-21-357-2021, 2021.

Lack, D. A. and Cappa, C. D.: Impact of brown and clear carbon on light absorption enhancement, single
scatter albedo and absorption wavelength dependence of black carbon, Atmos. Chem. Phys., 10,
920     4207-4220, 10.5194/acp-10-4207-2010, 2010.

Laskin, A., Laskin, J., and Nizkorodov, S. A.: Chemistry of Atmospheric Brown Carbon, Chemical
Reviews, 115, 4335-4382, 10.1021/cr5006167, 2015.

Leahy, L. V., Anderson, T. L., Eck, T. F., and Bergstrom, R. W.: A synthesis of single scattering albedo of biomass burning aerosol over southern Africa during SAFARI 2000, Geophysical Research Letters, 34, https://doi.org/10.1029/2007GL029697, 2007.

LeBlanc, S. E., Redemann, J., Flynn, C., Pistone, K., Kacenelenbogen, M., Segal-Rosenheimer, M., Shinozuka, Y., Dunagan, S., Dahlgren, R. P., Meyer, K., Podolske, J., Howell, S. G., Freitag, S., Small-Griswold, J., Holben, B., Diamond, M., Wood, R., Formenti, P., Piketh, S., Maggs-Kölling, G., Gerber, M., and Namwoonde, A.: Above-cloud aerosol optical depth from airborne observations in the southeast Atlantic, Atmos. Chem. Phys., 20, 1565-1590, 10.5194/acp-20-1565-2020, 2020.

Lenhardt, E. D., Gao, L., Redemann, J., Xu, F., Burton, S. P., Cairns, B., Chang, I., Ferrare, R. A., Hostetler, C. A., Saide, P. E., Howes, C., Shinozuka, Y., Stamnes, S., Kacarab, M., Dobracki, A., Wong, J., Freitag, S., and Nenes, A.: Use of lidar aerosol extinction and backscatter coefficients to estimate cloud condensation nuclei (CCN) concentrations in the southeast Atlantic, Atmos. Meas. Tech., 16, 2037-2054, 10.5194/amt-16-2037-2023, 2023.

Levin, E. J. T., McMeeking, G. R., Carrico, C. M., Mack, L. E., Kreidenweis, S. M., Wold, C. E., Moosmüller, H., Arnott, W. P., Hao, W. M., Collett Jr., J. L., and Malm, W. C.: Biomass burning smoke aerosol properties measured during Fire Laboratory at Missoula Experiments (FLAME), Journal of Geophysical Research: Atmospheres, 115, https://doi.org/10.1029/2009JD013601, 2010.

Liu, D., Li, S., Hu, D., Kong, S., Cheng, Y., Wu, Y., Ding, S., Hu, K., Zheng, S., Yan, Q., Zheng, H., Zhao, D., Tian, P., Ye, J., Huang, M., and Ding, D.: Evolution of Aerosol Optical Properties from Wood Smoke in Real Atmosphere Influenced by Burning Phase and Solar Radiation, Environmental Science & Technology, 55, 5677-5688, 10.1021/acs.est.0c07569, 2021.

Liu, S., Aiken, A. C., Arata, C., Dubey, M. K., Stockwell, C. E., Yokelson, R. J., Stone, E. A., Jayarathne, T., Robinson, A. L., DeMott, P. J., and Kreidenweis, S. M.: Aerosol single scattering albedo dependence on biomass combustion efficiency: Laboratory and field studies, Geophysical Research Letters, 41, 742-748, 10.1002/2013gl058392, 2014.

Ma, P.-L., Rasch, P. J., Fast, J. D., Easter, R. C., Gustafson Jr, W., Liu, X., Ghan, S. J., and Singh, B.: Assessing the CAM5 physics suite in the WRF-Chem model: Implementation, resolution sensitivity, and a first evaluation for a regional case study, Geoscientific Model Development, 7, 755-778, 2014.

Mallet, M., Solmon, F., Nabat, P., Elguindi, N., Waquet, F., Bouniol, D., Sayer, A. M., Meyer, K., Roehrig, R., Michou, M., Zuidema, P., Flamant, C., Redemann, J., and Formenti, P.: Direct and semi-direct radiative forcing of biomass-burning aerosols over the southeast Atlantic (SEA) and its sensitivity

to absorbing properties: a regional climate modeling study, Atmos. Chem. Phys., 20, 13191-13216, 10.5194/acp-20-13191-2020, 2020.

Meyer, K., Platnick, S., Oreopoulos, L., and Lee, D.: Estimating the direct radiative effect of absorbing aerosols overlying marine boundary layer clouds in the southeast Atlantic using MODIS and CALIOP, Journal of Geophysical Research: Atmospheres, 118, 4801-4815, https://doi.org/10.1002/jgrd.50449, 2013.

Mishra, A. K., Koren, I., and Rudich, Y.: Effect of aerosol vertical distribution on aerosol-radiation interaction: A theoretical prospect, Heliyon, 1, e00036, https://doi.org/10.1016/j.heliyon.2015.e00036, 2015.

Mitchell, L. T., Redemann, J., Pistone, K., LeBlanc, S., and Schmidt, S.: Subseasonal and Spatial Variability of Biomass Burning Aerosol Radiative Properties Observed over the Southeast Atlantic during ORACLES 2016-2018 by 4STAR, In-Situ, and the Southern African AERONET Extended Record, AGU23, San Francisco, CA2023.

Moosmüller, H., Engelbrecht, J. P., Skiba, M., Frey, G., Chakrabarty, R. K., and Arnott, W. P.: Single scattering albedo of fine mineral dust aerosols controlled by iron concentration, Journal of Geophysical Research: Atmospheres, 117, https://doi.org/10.1029/2011JD016909, 2012.

Nascimento, J. P., Bela, M. M., Meller, B. B., Banducci, A. L., Rizzo, L. V., Vara-Vela, A. L., Barbosa, H. M. J., Gomes, H., Rafee, S. A. A., Franco, M. A., Carbone, S., Cirino, G. G., Souza, R. A. F., McKeen, S. A., and Artaxo, P.: Aerosols from anthropogenic and biogenic sources and their interactions – modeling aerosol formation, optical properties, and impacts over the central Amazon basin, Atmos. Chem. Phys., 21, 6755-6779, 10.5194/acp-21-6755-2021, 2021.

ORACLES: ORACLES Science Team. ObseRvations of Aerosols above CLouds and their intEractionS. [dataset], https://doi.org/10.5067/SUBORBITAL/ORACLES/DATA001, 2020.

Pistone, K., Redemann, J., Doherty, S., Zuidema, P., Burton, S., Cairns, B., Cochrane, S., Ferrare, R., Flynn, C., Freitag, S., Howell, S. G., Kacenelenbogen, M., LeBlanc, S., Liu, X., Schmidt, K. S., Sedlacek Iii, A. J., Segal-Rozenhaimer, M., Shinozuka, Y., Stamnes, S., van Diedenhoven, B., Van Harten, G., and Xu, F.: Intercomparison of biomass burning aerosol optical properties from in situ and remote-sensing instruments in ORACLES-2016, Atmos. Chem. Phys., 19, 9181-9208, 10.5194/acp-19-9181-2019, 2019.

Queface, A. J., Piketh, S. J., Eck, T. F., Tsay, S.-C., and Mavume, A. F.: Climatology of aerosol optical properties in Southern Africa, Atmospheric Environment, 45, 2910-2921, https://doi.org/10.1016/j.atmosenv.2011.01.056, 2011.

Redemann, J., Russell, P. B., and Hamill, P.: Dependence of aerosol light absorption and single-scattering albedo on ambient relative humidity for sulfate aerosols with black carbon cores, Journal of

Geophysical Research: Atmospheres, 106, 27485-27495, https://doi.org/10.1029/2001JD900231, 2001.

Redemann, J., Wood, R., Zuidema, P., Doherty, S. J., Luna, B., LeBlanc, S. E., Diamond, M. S., Shinozuka, Y., Chang, I. Y., Ueyama, R., Pfister, L., Ryoo, J. M., Dobracki, A. N., da Silva, A. M., Longo, K. M., Kacenelenbogen, M. S., Flynn, C. J., Pistone, K., Knox, N. M., Piketh, S. J., Haywood, J. M., Formenti, P., Mallet, M., Stier, P., Ackerman, A. S., Bauer, S. E., Fridlind, A. M., Carmichael, G. R., Saide, P. E., Ferrada, G. A., Howell, S. G., Freitag, S., Cairns, B., Holben, B. N., Knobelspiesse, K. D., Tanelli, S., L'Ecuyer, T. S., Dzambo, A. M., Sy, O. O., McFarquhar, G. M., Poellot, M. R., Gupta, S., O'Brien, J. R., Nenes, A., Kacarab, M., Wong, J. P. S., Small-Griswold, J. D., Thornhill, K. L., Noone, D., Podolske, J. R., Schmidt, K. S., Pilewskie, P., Chen, H., Cochrane, S. P., Sedlacek, A. J., Lang, T. J., Stith, E., Segal-Rozenhaimer, M., Ferrare, R. A., Burton, S. P., Hostetler, C. A., Diner, D. J., Seidel, F. C., Platnick, S. E., Myers, J. S., Meyer, K. G., Spangenberg, D. A., Maring, H., and Gao, L.: An overview of the ORACLES (ObseRvations of Aerosols above CLouds and their intEractionS) project: aerosol–cloud–radiation interactions in the southeast Atlantic basin, Atmos. Chem. Phys., 21, 1507-1563, 10.5194/acp-21-1507-2021, 2021.

Reid, J. S., Hobbs, P. V., Ferek, R. J., Blake, D. R., Martins, J. V., Dunlap, M. R., and Liousse, C.: Physical, chemical, and optical properties of regional hazes dominated by smoke in Brazil, Journal of Geophysical Research: Atmospheres, 103, 32059-32080, https://doi.org/10.1029/98JD00458, 1998.

Ryoo, J. M., Pfister, L., Ueyama, R., Zuidema, P., Wood, R., Chang, I., and Redemann, J.: A meteorological overview of the ORACLES (ObseRvations of Aerosols above CLouds and their intEractionS) campaign over the southeastern Atlantic during 2016–2018: Part 1 – Climatology, Atmos. Chem. Phys., 21, 16689-16707, 10.5194/acp-21-16689-2021, 2021.

Saide, P. E., Thompson, G., Eidhammer, T., da Silva, A. M., Pierce, R. B., and Carmichael, G. R.: Assessment of biomass burning smoke influence on environmental conditions for multi-year tornado outbreaks by combining aerosol-aware microphysics and fire emission constraints, J Geophys Res Atmos, 121, 10294-10311, 10.1002/2016JD025056, 2016.

Sakaeda, N., Wood, R., and Rasch, P. J.: Direct and semidirect aerosol effects of southern African biomass burning aerosol, Journal of Geophysical Research: Atmospheres, 116, https://doi.org/10.1029/2010JD015540, 2011.

Saleh, R., Marks, M., Heo, J., Adams, P. J., Donahue, N. M., and Robinson, A. L.: Contribution of brown carbon and lensing to the direct radiative effect of carbonaceous aerosols from biomass and biofuel burning emissions, Journal of Geophysical Research: Atmospheres, 120, 10,285-210,296, https://doi.org/10.1002/2015JD023697, 2015.

1025     Samset, B. H., Stjern, C. W., Andrews, E., Kahn, R. A., Myhre, G., Schulz, M., and Schuster, G. L.: Aerosol Absorption: Progress Towards Global and Regional Constraints, Current Climate Change Reports, 4, 65-83, 10.1007/s40641-018-0091-4, 2018.

Santer, B. D., Taylor, K. E., Wigley, T. M. L., Johns, T. C., Jones, P. D., Karoly, D. J., Mitchell, J. F. B., Oort, A. H., Penner, J. E., Ramaswamy, V., Schwarzkopf, M. D., Stouffer, R. J., and Tett, S.: A
1030     search for human influences on the thermal structure of the atmosphere, Nature, 382, 39-46, 10.1038/382039a0, 1996.

Satheesh, S. K., Vinoj, V., and Krishna Moorthy, K.: Radiative effects of aerosols at an urban location in southern India: Observations versus model, Atmospheric Environment, 44, 5295-5304, https://doi.org/10.1016/j.atmosenv.2010.07.020, 2010.

1035     Schuster, G. L., Dubovik, O., and Holben, B. N.: Angstrom exponent and bimodal aerosol size distributions, Journal of Geophysical Research: Atmospheres, 111, https://doi.org/10.1029/2005JD006328, 2006.

Sedlacek, A. J., III, Lewis, E. R., Onasch, T. B., Zuidema, P., Redemann, J., Jaffe, D., and Kleinman, L. I.: Using the Black Carbon Particle Mixing State to Characterize the Lifecycle of Biomass Burning
1040     Aerosols, Environmental Science & Technology, 56, 14315-14325, 10.1021/acs.est.2c03851, 2022.

Shinozuka, Y., Kacenelenbogen, M. S., Burton, S. P., Howell, S. G., Zuidema, P., Ferrare, R. A., LeBlanc, S. E., Pistone, K., Broccardo, S., Redemann, J., Schmidt, K. S., Cochrane, S. P., Fenn, M., Freitag, S., Dobracki, A., Segal-Rosenheimer, M., and Flynn, C. J.: Daytime aerosol optical depth above
1045     low-level clouds is similar to that in adjacent clear skies at the same heights: airborne observation above the southeast Atlantic, Atmos. Chem. Phys., 20, 11275-11285, 10.5194/acp-20-11275-2020, 2020b.

Shinozuka, Y., Saide, P. E., Ferrada, G. A., Burton, S. P., Ferrare, R., Doherty, S. J., Gordon, H., Longo, K., Mallet, M., Feng, Y., Wang, Q., Cheng, Y., Dobracki, A., Freitag, S., Howell, S. G., LeBlanc,
1050     S., Flynn, C., Segal-Rosenhaimer, M., Pistone, K., Podolske, J. R., Stith, E. J., Bennett, J. R., Carmichael, G. R., da Silva, A., Govindaraju, R., Leung, R., Zhang, Y., Pfister, L., Ryoo, J. M., Redemann, J., Wood, R., and Zuidema, P.: Modeling the smoky troposphere of the southeast Atlantic: a comparison to ORACLES airborne observations from September of 2016, Atmos. Chem. Phys., 20, 11491-11526, 10.5194/acp-20-11491-2020, 2020a.

1055     Sinyuk, A., Holben, B. N., Eck, T. F., Giles, D. M., Slutsker, I., Korkin, S., Schafer, J. S., Smirnov, A., Sorokin, M., and Lyapustin, A.: The AERONET Version 3 aerosol retrieval algorithm, associated uncertainties and comparisons to Version 2, Atmos. Meas. Tech., 13, 3375-3411, 10.5194/amt-13-3375-2020, 2020.

Smirnov, A., Holben, B. N., Kaufman, Y. J., Dubovik, O., Eck, T. F., Slutsker, I., Pietras, C., and Halthore, R. N.: Optical Properties of Atmospheric Aerosol in Maritime Environments, Journal of the Atmospheric Sciences, 59, 501-523, https://doi.org/10.1175/1520-0469(2002)059<0501:OPOAAI>2.0.CO;2, 2002.

Stein, A. F., Draxler, R. R., Rolph, G. D., Stunder, B. J. B., Cohen, M. D., and Ngan, F.: NOAA's HYSPLIT Atmospheric Transport and Dispersion Modeling System, Bulletin of the American Meteorological Society, 96, 2059-2077, https://doi.org/10.1175/BAMS-D-14-00110.1, 2015.

Stier, P., Schutgens, N. A. J., Bellouin, N., Bian, H., Boucher, O., Chin, M., Ghan, S., Huneeus, N., Kinne, S., Lin, G., Ma, X., Myhre, G., Penner, J. E., Randles, C. A., Samset, B., Schulz, M., Takemura, T., Yu, F., Yu, H., and Zhou, C.: Host model uncertainties in aerosol radiative forcing estimates: results from the AeroCom Prescribed intercomparison study, Atmos. Chem. Phys., 13, 3245-3270, 10.5194/acp-13-3245-2013, 2013.

Takemura, T., Nakajima, T., Dubovik, O., Holben, B. N., and Kinne, S.: Single-Scattering Albedo and Radiative Forcing of Various Aerosol Species with a Global Three-Dimensional Model, Journal of Climate, 15, 333-352, https://doi.org/10.1175/1520-0442(2002)015<0333:SSAARF>2.0.CO;2, 2002.

Tatro, T. and Zuidema, P.: More biomass burning aerosol is being advected westward over the southern tropical Atlantic since 2003, Science of The Total Environment, 965, 178506, https://doi.org/10.1016/j.scitotenv.2025.178506, 2025.

Taylor, J. W., Wu, H., Szpek, K., Bower, K., Crawford, I., Flynn, M. J., Williams, P. I., Dorsey, J., Langridge, J. M., Cotterell, M. I., Fox, C., Davies, N. W., Haywood, J. M., and Coe, H.: Absorption closure in highly aged biomass burning smoke, Atmos. Chem. Phys., 20, 11201-11221, 10.5194/acp-20-11201-2020, 2020.

Thompson, G. and Eidhammer, T.: A Study of Aerosol Impacts on Clouds and Precipitation Development in a Large Winter Cyclone, Journal of the Atmospheric Sciences, 71, 3636-3658, 10.1175/jas-d-13-0305.1, 2014.

Twomey, S.: Pollution and the planetary albedo, Atmospheric Environment (1967), 8, 1251-1256, https://doi.org/10.1016/0004-6981(74)90004-3, 1974.

Twomey, S.: The Influence of Pollution on the Shortwave Albedo of Clouds, Journal of Atmospheric Sciences, 34, 1149-1152, 10.1175/1520-0469(1977)034<1149:Tiopot>2.0.Co;2, 1977.

Vakkari, V., Beukes, J. P., Dal Maso, M., Aurela, M., Josipovic, M., and van Zyl, P. G.: Major secondary aerosol formation in southern African open biomass burning plumes, Nature Geoscience, 11, 580-583, 10.1038/s41561-018-0170-0, 2018.

van der Werf, G. R., Randerson, J. T., Giglio, L., Collatz, G. J., Mu, M., Kasibhatla, P. S., Morton, D. C., DeFries, R. S., Jin, Y., and van Leeuwen, T. T.: Global fire emissions and the contribution of deforestation, savanna, forest, agricultural, and peat fires (1997–2009), Atmos. Chem. Phys., 10, 11707-11735, 10.5194/acp-10-11707-2010, 2010.

Vermote, E., Ellicott, E., Dubovik, O., Lapyonok, T., Chin, M., Giglio, L., and Roberts, G. J.: An approach to estimate global biomass burning emissions of organic and black carbon from MODIS fire radiative power, Journal of Geophysical Research: Atmospheres, 114, https://doi.org/10.1029/2008JD011188, 2009.

Wang, Y., Vogel, J. M., Lin, Y., Pan, B., Hu, J., Liu, Y., Dong, X., Jiang, J. H., Yung, Y. L., and Zhang, R.: Aerosol microphysical and radiative effects on continental cloud ensembles, Advances in Atmospheric Sciences, 35, 234-247, 10.1007/s00376-017-7091-5, 2018.

Waquet, F., Peers, F., Ducos, F., Goloub, P., Platnick, S., Riedi, J., Tanré, D., and Thieuleux, F.: Global analysis of aerosol properties above clouds, Geophysical Research Letters, 40, 5809-5814, https://doi.org/10.1002/2013GL057482, 2013.

Wilcox, E. M.: Direct and semi-direct radiative forcing of smoke aerosols over clouds, Atmos. Chem. Phys., 12, 139-149, 10.5194/acp-12-139-2012, 2012.

Wu, H., Taylor, J. W., Szpek, K., Langridge, J. M., Williams, P. I., Flynn, M., Allan, J. D., Abel, S. J., Pitt, J., Cotterell, M. I., Fox, C., Davies, N. W., Haywood, J., and Coe, H.: Vertical variability of the properties of highly aged biomass burning aerosol transported over the southeast Atlantic during CLARIFY-2017, Atmos. Chem. Phys., 20, 12697-12719, 10.5194/acp-20-12697-2020, 2020.

Zhang, J. and Zuidema, P.: The diurnal cycle of the smoky marine boundary layer observed during August in the remote southeast Atlantic, Atmos. Chem. Phys., 19, 14493-14516, 10.5194/acp-19-14493-2019, 2019.

Zhang, J. and Zuidema, P.: Sunlight-absorbing aerosol amplifies the seasonal cycle in low-cloud fraction over the southeast Atlantic, Atmos. Chem. Phys., 21, 11179-11199, 10.5194/acp-21-11179-2021, 2021.

Zhang, Y., Chen, Y., Fan, J., and Leung, L.-Y. R.: Application of an Online-Coupled Regional Climate Model, WRF-CAM5, over East Asia for Examination of Ice Nucleation Schemes: Part II. Sensitivity to Heterogeneous Ice Nucleation Parameterizations and Dust Emissions, Climate, 3, 753-774, 2015b.

Zhang, Y., Zhang, X., Wang, K., He, J., Leung, L. R., Fan, J., and Nenes, A.: Incorporating an advanced aerosol activation parameterization into WRF-CAM5: Model evaluation and parameterization intercomparison, Journal of Geophysical Research: Atmospheres, 120, 6952-6979, https://doi.org/10.1002/2014JD023051, 2015a.

Zhou, S., Collier, S., Jaffe, D. A., Briggs, N. L., Hee, J., Sedlacek Iii, A. J., Kleinman, L., Onasch, T. B., and Zhang, Q.: Regional influence of wildfires on aerosol chemistry in the western US and insights into atmospheric aging of biomass burning organic aerosol, Atmos. Chem. Phys., 17, 2477-2493, 10.5194/acp-17-2477-2017, 2017.

1130 Zuidema, P., Redemann, J., Haywood, J., Wood, R., Piketh, S., Hipondoka, M., and Formenti, P.: Smoke and Clouds above the Southeast Atlantic: Upcoming Field Campaigns Probe Absorbing Aerosol's Impact on Climate, Bulletin of the American Meteorological Society, 97, 1131-1135, 10.1175/bams-d-15-00082.1, 2016.

Zuidema, P., Sedlacek III, A. J., Flynn, C., Springston, S., Delgadillo, R., Zhang, J., Aiken, A. C., Koontz,
1135 A., and Muradyan, P.: The Ascension Island Boundary Layer in the Remote Southeast Atlantic is Often Smoky, Geophysical Research Letters, 45, 4456-4465, https://doi.org/10.1002/2017GL076926, 2018.